The Astrophysical Journal, 970:190 (32pp), 2024 August 1 https://doi.org/10.3847/1538-4357/ad47c2

The Nature of X-Rays from Young Stellar Objects in the Orion Nebula Cluster—A Chandra HETGS Legacy Project

Norbert S. Schulz[1], David P. Huenemoerder[1], David A. Principe[1], Marc Gagne[2], Hans Moritz Günther[1], Joel Kastner[3], Joy Nichols[4], Andrew Pollock[5], Thomas Preibisch[6], Paola Testa[4], Fabio Reale[7], Fabio Favata[8,9], and Claude R. Canizares[1]

[1] Department of Physics and Kavli Institute for Astrophysics and Space Research, Massachusetts Institute of Technology, Cambridge, MA 02139, USA
[2] West Chester University, West Chester, PA 19383, USA
[3] Center for Imaging Science, School of Physics & Astronomy, and Laboratory for Multiwavelength Astrophysics, Rochester Institute of Technology, 54 Lomb Memorial Drive, Rochester, NY 14623, USA
[4] Harvard & Smithsonian Center for Astrophysics, Cambridge, MA 02138, USA
[5] Department of Physics and Astronomy, University of Sheffield, Sheffield S10 2TN, UK
[6] Universitäts-Sternwarte München, Ludwig-Maximilians-Universität, 81679 München, Germany
[7] University of Palermo, 90133 Palermo, Italy
[8] ESA European Space Research and Technology Centre (ESTEC), Keplerlaan 1, 2201 AZ Noordwijk, The Netherlands
[9] INAF—Osservatorio Astronomico di Palermo, Piazza del Parlamento 1, 90134 Palermo, Italy
Received 2023 November 16; revised 2024 April 21; accepted 2024 April 23; published 2024 July 31

Abstract

The Orion Nebula Cluster (ONC) is the closest site of very young (∼1 Myr) massive star formation The ONC hosts more than 1600 young and X-ray bright stars with masses ranging from ∼0.1–35 $M_{\odot}$. The Chandra HETGS Orion Legacy Project observed the ONC with the Chandra High Energy Transmission Grating Spectrometer (HETGS) for 2.1 Ms. We describe the spectral extraction and cleaning processes necessary to separate overlapping spectra. We obtained 36 high-resolution spectra, which include a high-brilliance X-ray spectrum of θ^1 Ori C with over 100 highly significant X-ray lines. The lines show Doppler broadening between 300 and 400 km s^{-1}. Higher spectral diffraction orders allow us to resolve line components of high Z He-like triplets in θ^1 Ori C with unprecedented spectral resolution. Long-term light curves spanning ∼20 yr show all stars to be highly variable, including the massive stars. Spectral fitting with thermal coronal emission line models reveals that most sources show column densities of up to a few times 10^{22} cm^{-2} and high coronal temperatures of 10–90 MK. We observe a bifurcation of the high-temperature component where some stars show a high component of 40 MK, while others show above 60 MK, indicating heavy flaring activity. Some lines are resolved with Doppler broadening above our threshold of ∼200 km s^{-1}, up to 500 km s^{-1}. This data set represents the largest collection of HETGS high-resolution X-ray spectra from young pre-main-sequence stars in a single star-forming region to date.

Unified Astronomy Thesaurus concepts: Pre-main sequence stars (1290); X-ray stars (1823); High resolution spectroscopy (2096)

Materials only available in the online version of record: animation, data behind figures, interactive figures

1. Introduction

The Orion Nebula Cluster (ONC) is a very young star-forming region hosting a large number of young stellar objects in terms of mass, age, and evolutionary stages. The cluster is part of the Orion A molecular cloud hosting a hierarchical structure of ongoing star formation cells (Bally et al. 2000). The part of this region we generally refer to as the ONC is a somewhat older formation bubble located at the foreground of the main molecular cloud. Two very massive stars—θ^1 Ori C and θ^2 Ori A—are members of the Orion Trapezium Cluster at the core of the ONC, with θ^1 Ori C being the main source of illumination and ionization of the Orion Nebula (M42). The ONC also hosts a large assembly of young stars, with about 80% of its members being younger than a few million years. With over 3000 stars in the vicinity of the Orion Trapezium, the average stellar density amounts to about 250 stars per cubic parsec within a radius of about 3 pc (Hillenbrand 1997). The ONC is the nearest site of massive star formation rich in a low- and intermediate-mass pre-main-sequence (PMS) stellar population as well as early-type zero-age main-sequence stars. It is well studied in the optical and infrared bands, with about 1600 sources classified to some limited extent through spectroscopic and photometric measurements (Hillenbrand 1997; Hillenbrand et al. 2013) and over 2000 stars being observed in the IR band with Two Micron All Sky Survey (2MASS; Skrutskie et al. 2006) and ground-based surveys (Muench et al. 2002; Robberto et al. 2010; Manara et al. 2012).

The ONC also has a long history of X-ray observations. From its first discovery with Uhuru (Giacconi et al. 1972) identified as a bright X-ray source 3U0527-05 to the realization that this is a more extended emission region containing X-rays from stellar coronae around young T Tauri stars (den Boggende et al. 1978; Feigelson & Decampli 1981; Gagne et al. 1995), decades of observations established the ONC as one of the richest X-ray emitting star-forming clusters. However, while most of these studies were severely limited by the low-angular resolution of their satellite telescopes, ROSAT in the 1990s came in best with 5″, a true breakthrough came with the launch of Chandra in 1999, which then offered an angular resolution

of 0.″5–2″ over a few arcminute field of view. The Chandra Orion Ultradeep Project (COUP; Feigelson et al. 2005) took full advantage of this superb observing capability and observed the ONC for nearly 10 days total to detect 1616 X-ray sources, measure column densities, source fluxes, and basic X-ray spectral and photometric parameters (Getman et al. 2005). Many X-ray surveys of other young stellar clusters were performed with Chandra, examples are RCW38 (Wolk et al. 2006), 30 Doradus (Townsley et al. 2006), NGC 6357 (Wang et al. 2007), M17 (Broos et al. 2007), NGC 2244 (Wang et al. 2008), or recently in the Tarantula Nebula (Crowther et al. 2022). Perhaps the most notable survey is the large Chandra Carina Complex Project, which detected over 14,000 X-ray sources with a large number of multiwavelength counterparts (Townsley et al. 2011; Broos et al. 2011; Gagné et al. 2011; Feigelson et al. 2011; Preibisch et al. 2011).

Young, low-mass (0.1–2 $M_{\odot}$) PMS stars are brighter in X-rays than their more evolved counterparts on the main sequence. The ratio of X-ray to bolometric luminosity in these stars lies between 10^{-4} and 10^{-3}, close to the saturation threshold (Vilhu 1984; Vilhu & Walter 1987; Wright et al. 2011). Besides coronal activity, accretion and outflows can also contribute X-ray flux for those stars still surrounded by a protoplanetary disk (for a review, see Schneider et al. 2022). Those stars are called classical T Tauri stars (CTTS). X-rays from shocks in outflows are very soft and orders of magnitude fainter than coronal emission (Güdel et al. 2011); they can generally only be seen in nearby stars with little absorption where the jet is spatially resolved. One of the first detections of soft X-rays from shocks at the base of an outflow was an Orion proplyd using the COUP data set (Kastner et al. 2005). Another source of X-rays is the accretion shock itself. The disk does not reach down to the star, but instead, mass falls onto the stellar surface along the magnetic field lines. It is accelerated to freefall velocities and forms a strong shock at the stellar surface. This shock heats the infalling gas to X-ray emitting temperatures (Lamzin 1998; Günther et al. 2007; Hartmann et al. 2016). The density in the shock is high enough that it alters the line ratios in the He-like triplets, which are resolved in high-resolution X-ray grating spectroscopy (e.g., Kastner et al. 2002, 2004; Testa et al. 2004; Schmitt et al. 2005; Günther et al. 2006; Argiroffi et al. 2007, 2012; Brickhouse et al. 2010). However, it is not clear if it is actually the shock itself that is observed (Reale et al. 2013, 2014), or if the depth of the shock in the photosphere and the outer layers of an inhomogeneous accretion column hide the shock from view (Sacco et al. 2010; Schneider et al. 2018; Espaillat et al. 2021), and the observed line ratios would be a secondary effect, formed where cooler and denser plasma flows up into the corona as seen in simulations (Orlando et al. 2010, 2013).

Older weak-lined T Tauri stars (WTTS) do not show accretion and thus have coronal line ratios in their He-like triplets, e.g., in the WTTS HID 98890 (e.g., Kastner et al. 2004). Telleschi et al. (2007) also showed that many CTTS have hard spectra with substantial emissions up to 10 keV, far beyond the reach of accretion shock heated plasma. Yet, in the accretion phase, the stars accrete not only mass, but also angular momentum; young stars, CTTS, and WTTS, thus rotate faster than their older main-sequence counterparts, which explains the saturated level of coronal activity. This fact is often used to identify young stars in a dense field, e.g., Pillitteri et al. (2013) use X-ray observations in the Orion A cloud south of the ONC to find young, but disk-less cluster members.

Performing high spectral resolution X-ray studies of very young stellar clusters is challenging. The Chandra High Energy Resolution Transmission Grating Spectrometer (HETGS) disperses the image of a point source across the field of view (see Canizares et al. 2000). This works well for isolated objects, but is susceptible to confusion from intersecting and overlapping spectra in crowded fields, such as young stellar associations. HETGS spectra of the close by TW Hydra association were easy to obtain because the member stars are sufficiently well separated in individual pointings (Kastner et al. 2002, 2004; Huenemoerder et al. 2007). Stars of the Cygnus OB2 association fit into one single pointing, but they are still sufficiently well separated to prevent serious confusion (Waldron et al. 2004).

The ONC is the nearest massive star-forming cluster at a distance of ≃400 pc (Menten et al. 2007; Kounkel et al. 2017; Kuhn et al. 2019; Maíz Apellániz et al. 2022). Its brightest sources were a focus early in the Chandra mission, involving θ^1 Ori A, C, and E (Schulz et al. 2003; Gagné et al. 2005; Huenemoerder et al. 2009), and θ^2 Ori A (Schulz et al. 2006; Mitschang et al. 2011). Schulz et al. (2015) used an early set of Chandra HETG observations to study six bright PMS stars in the near environment of the Orion Trapezium at the core of the ONC. Here, significant confusion between overlapping spectra was encountered. That study specified the limitations of high angular resolution as offered by the Chandra optics and dispersive high-resolution spectroscopy offered by the HETGS. In the ONC field of view, the closest separation within bright sources is between 5″ and 8″, which appeared to make a deep high-resolution study feasible. However, it also indicated that even though the angular resolution of Chandra is 0.″5, dispersive studies of PMS stars separated by less than 3″–5″ are not feasible. The study by Huenemoerder et al. (2007) of Hen 3-600 shows this limitation well for a 1.″5 binary. This excludes all clusters more distant than the ONC.

In this pilot paper, we describe our observation of the ONC with the Chandra HETGS in order to obtain more than three dozen high-resolution X-ray grating spectra of ONC member stars. The data described in this pilot paper are made public and we anticipate several science publications to follow by the authors and the science community. We present observations, spectral confusion cleaning procedures, a set of final spectra bearing a total number of counts and exposure time after spectral cleaning, and a first in-depth analysis of the X-ray properties of massive, intermediate-mass stars and low-mass PMS stars in the ONC for which we have sufficient spectral data. Any follow-up paper should then refer to this pilot paper and the official data release site for a full description of the data.

2. Observations and Data Reduction

2.1. The Chandra HETGS

The Chandra HETG assembly consists of an array of periodic gold microstructures that can be interposed in the converging X-ray beam just behind the Chandra High Resolution Mirror Assembly. When the telescope observes a point source with the gratings in place, a fraction of the X-rays are dispersed, according to wavelength, to either side of the point source zeroth-order image. The zeroth-order image and

the dispersed ± first and less prominent higher orders are detected at the focal plane by the linear array of charge-coupled devices (CCD) detectors, ACIS-S. Thus, the whole system of mirror, gratings, and detector constitutes a slitless spectrometer, the HETGS (Canizares et al. 2000). The HETG assembly has two different grating types, designated Medium Energy Grating (MEG) and High Energy Grating (HEG), optimized for medium and high energies, respectively. The gratings are mounted so that the dispersed ± spectra of the MEG and HEG are offset from one another by an angle of 10°, forming a shallow "X" in the focal plane with the zeroth-order image at its center.

The HETGS provides spectral resolving powers of $\lambda/\Delta\lambda =$ 100–1000 in its first orders for point sources, corresponding to a line FWHM of about 0.02 Å for MEG and 0.01 Å for HEG, and effective areas of 1–180 cm^2 over the wavelength range of 1.2–30 Å (0.4–10 keV). Multiple overlapping orders are separated using the moderate-energy resolution of ACIS-S.

2.2. HETGS Observations

The data contains a set of 70 observations of the ONC with the HETG aimed at the central star of the Orion Trapezium θ^1 Ori C, obtained by the Chandra X-ray Observatory, contained in the Chandra Data Collection 192.[10] The total amount of the exposure is 2086.14 ks taken over a period of about 20 yr. The top right inset of Figure 1 shows the merged image of all observations over the most effective field of view summed over all roll angles. Nearly all visible dispersive HETG streaks are due to the three brightest sources in the field, θ^1 Ori C, θ^1 Ori E, and MT Ori. The observations are divided into two observation periods: one taken over 6 yr after the launch of Chandra in 1999 up to the year 2007, amounting to 470.96 ks and a second one during the years 2019 and 2020, amounting to a total of 1615.18 ks all summarized in Table 1.

The first period of observations used the full array of ACIS-S CCDs. This means for these data, full access to the Chandra wavelength band is available from 1.70–30 Å. These observations also provide the bulk of X-rays above 16 Å due to progressing ACIS contamination at later stages in the Chandra mission.

The second period of observations happened about 13 yr later after the observing conditions of the satellite had changed. Progressing contamination of the focal plane CCD array optical blocking filter effectively blocks soft X-rays below 1 keV (>12.3485 Å). In addition, thermal constraints due to the deteriorating thermal protection of the spacecraft require reducing the number of CCD devices activated during observations. With six CCDs, we have the full wavelength band available; with five CCDs, this still holds, but we lose some exposure above about 24 Å; with four CCDs, we lose exposure above about 18 Å. This is not an additional limitation, however, as the progressive ACIS filter contamination blocks most of the exposure above 16 Å anyway.

2.3. Spectral Extraction

For most data preparation and spectral analysis, we used the Interactive Spectral Interpretation System (ISIS; Houck & Denicola 2000). To uniformly process the many observations, each with multiple objects of interest in a crowded field, we modified the standard procedures of the `CIAO` software (Fruscione et al. 2006). Events were rerun through standard event processing to update bad pixel maps and to *destreak* bad events on CCD_ID 8 (ACIS-S4). We then reran `acis_process_events` to recreate a Level 1 event file identical to what is done in standard processing. Since we have many observations with an ensemble of sources of interest in a crowded field, we matched and updated the World Coordinate System (WCS). This is so that we can run source spectral extractions using a priori source celestial coordinates from COUP (Getman et al. 2005). This avoids small position uncertainties in zeroth-order detection due to low exposure or confusion by dispersed spectra. We then simply skip the detection step and map the celestial coordinates to sky pixel for each observation using the WCS. In order to provide the WCS registration, we ran a `CIAO` source detection program, `wavdetect`, on the central region over an 8′ radius for several spatial scales. For that, we used a point spread function (PSF) map, which we created using `mkpsfmap` at 2.3 keV for an enclosed count fraction of 0.9. We then applied `wcs_match` to fit the rotation and translation of the coordinate system of each ObsID relative to COUP, and updated all Level 1 event files and corresponding aspect solution files with these solutions. Spectral extraction then followed the usual `CIAO` steps but with narrower than default cross-dispersion extraction regions (2″ full width instead of the default 4) to reduce the overlap of crossing HEG or MEG orders from different sources. This does not change the overall spectral extraction process, but reduces the ambiguity about from which source an event originates in the extraction mask. The aperture efficiency is reduced a bit, by about 5% at 6 Å, and by about 8% at 12 Å, but this was seen to significantly reduce the number of contaminated sources at a small loss of signal.

Responses were made in the usual way for each source extraction via the `CIAO` commands `mkgrmf` and `mkgarf`. While Ancillary Response Files (ARFs) depend critically on source position and observation details (such as the aspect history), Response Matrix Files (RMFs) do not. The RMFs depend on the spectral extraction region width, which we chose to be the same for all sources and observations. Thus, there are only four unique RMFs for HEG and MEG ±1 orders for all sources.

2.4. Confusion Analysis

The region of the sky observed by the HETGS includes more than 1000 known X-ray sources (Figure 1) and the majority of these are present in the field of view of individual epochs. The HETGS instrument disperses light from each X-ray source in a characteristic, shallow "X" shape on the ACIS-S detectors.[11] The non-dispersed (zeroth-order) events are located at the R.A. and decl. of the X-ray source in the sky. The first-, second-, and third-order events for each source are dispersed by an angle given by the dispersion equation. The orders overlap along a line, one pair for the ± HEG and one for the ± MEG. While every X-ray source in an HETGS field of view has its light dispersed in the characteristic X-shaped pattern, only those sources that are sufficiently bright will disperse enough events to yield meaningful spectra.

HETGS observations of crowded fields, where multiple bright point sources cast their X-shaped patterns on the CCDs,

[10] doi:10.25574/cdc.192

[11] https://cxc.harvard.edu/proposer/POG/

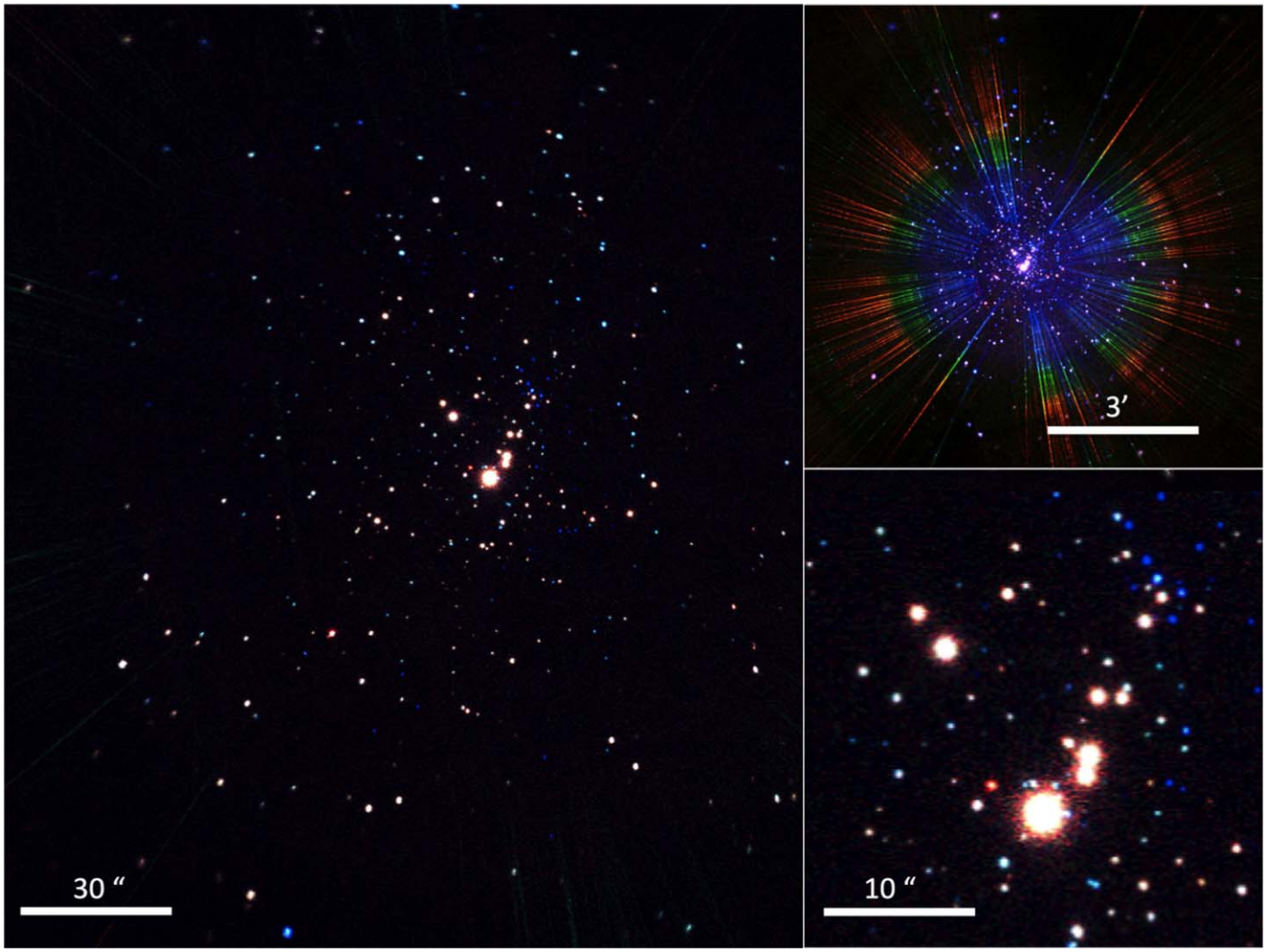

Figure 1. Merged zero-order image over the entire exposure using a three-color, red, green, and blue, scheme reflecting the stars' energy spectra. The main image is shown with a 30″ scale covering about 60% of the entire captured ACIS-S field of view. The dispersive HETG first- and higher-order dispersion events of the brightest star θ^1 Ori C were removed. The top right inset shows a wider view for 3′ with all dispersion streaks included. The most prominent ones are from θ^1 Ori C. The bottom right inset shows a zoomed version of the Orion Trapezium region, which includes about 10 of the brightest stars in the region and for which we have the most significant HETG first-order spectra.

suffer from event confusion, a scenario where events from two (or more) astrophysical sources could arrive at the same location on the detector and be erroneously assigned with standard `CIAO` processing (Figure 2, top). The relative locations of the dispersed spectra for each source depend on the roll angle of the observation. Dispersed spectra roll with the spacecraft, but zeroth-order sky positions do not. Hence, the relative positions of spectra change with roll and every epoch in the ONC HETGS data set will have unique sources of confusion (Figure 1). To identify and account for all the potential sources of confusion when extracting spectra, we created a custom Python program called `CrissCross`, which utilizes the fixed geometry of the X-shaped spectral dispersion region and the known location of X-ray sources in the field of view to produce un-confused spectra. While the details of `CrissCross` will be published in a forthcoming paper (D. Principe et al. 2024, in preparation), we summarize its utility here.

In the ONC HETGS data set, there are three primary causes of confusion when assigning events to a specific source for spectral extraction: (a) zeroth-order (non-dispersed) point sources falling on an extracted source spectral arm, (b) dispersed events from one source intersecting the arm of an extracted source, and (c) a bright source whose zeroth order lands on or near another source's spectral arm dispersing its events along the same location on the CCD (Figure 2, left). The location where confusion occurs in the spectrum of an extracted source is straightforward to calculate using the location on the CCD of the confuser and the well-calibrated energy to dispersion distance relation for HEG and MEG.

Standard `CIAO` processing already mitigates some portion of confusion by utilizing ACIS order sorting (Figure 2, right). When events are assigned to a specific source during spectral extraction, the CCD-resolved event energy is compared to the expected energy of the event based on its dispersion distance (i.e., the distance from the zeroth order in the dispersion direction). If these energies do not match within an energy range based on the spectral energy resolution of the CCD, then events from a confusing source will automatically be rejected from the extracted spectrum, effectively removing confusion. However, in a region with a large number of X-ray sources like the ONC, there are often cases where the CCD-resolved energy

Table 1
CHANDRA HETGS Observations

Obsid	Exp. (ks)	Date (UT)	Time (UT)	CCDs	MJD (days)
3	49.62	1999:10-31	05:47:21	6	51482.2
4	30.92	1999-11-24	05:37:54	6	51506.2
2567	46.36	2001-12-28	12:25:56	6	52271.5
2568	46.34	2002-01-19	20:29:42	6	52324.9
7407	24.64	2006-12-03	19:07:48	6	54072.8
7408	24.98	2006-12-19	14:17:30	6	54075.5
7409	27.09	2006-12-23	00:47:40	6	54088.6
7410	13.10	2006-12-06	12:11:37	6	54092.0
7411	24.64	2007-07-27	20:41:22	6	54308.9
7412	25.20	2007-07-28	06:16:09	6	54309.3
8568	36.08	2007-08-06	06:54:08	6	54318.3
8589	50.71	2007-08-08	21:30:35	6	54320.9
8895	24.97	2007-12-07	03:14:07	6	54419.4
8896	22.66	2007-11-30	21:58:31	6	54434.8
8897	23.65	2007-11-15	10:03:16	6	54441.1
23008	47.43	2019-11-27	12:07:33	4	58814.5
22893	24.73	2019-12-02	17:18:23	5	58819.7
22994	24.73	2019-12-05	09:22:57	4	58822.4
23087	39.54	2019-12-08	16:56:56	4	58825.7
22904	36.58	2019-12-10	17:49:59	4	58827.7
23097	35.88	2019-12-11	12:12:24	4	58828.5
22337	37.66	2019-12-13	04:25:33	4	58830.2
23006	24.73	2019-12-14	06:35:20	5	58831.3
22343	24.73	2019-12-15	20:04:15	4	58832.8
23003	24.74	2019-12-21	05:12:39	4	58838.2
23104	24.73	2019-12-21	21:47:04	5	58838.9
22336	25.59	2019-12-22	11:01:50	4	58839.5
23007	37.41	2019-12-24	23:12:06	4	58842.0
22339	31.64	2019-12-26	02:06:17	4	58843.1
22892	30.66	2019-12-26	22:46:53	4	58843.9
22995	38.74	2019-12-27	14:29:16	4	58844.6
22338	39.15	2019-12-30	06:02:12	4	58847.3
22334	24.73	2019-12-31	09:17:51	4	58849.3
23000	42.50	2020-01-01	07:04:24	4	58851.7
22996	26.70	2020-01-03	00:38:17	5	58852.4
23114	37.56	2020-01-03	16:46:28	4	58855.0
23115	29.67	2020-01-04	10:02:01	4	58856.5
22335	29.67	2020-01-06	23:19:34	4	58859.55
23005	24.73	2020-01-08	10:14:19	5	58941.05
23120	39.54	2020-01-11	12:12:26	4	58941.6
23012	10.81	2020-04-01	23:58:25	6	58943.9
23206	17.71	2020-04-02	13:57:51	6	58944.4
23207	14.75	2020-04-04	12:21:33	6	58948.4
23208	14.75	2020-04-05	08:54:30	6	58951.0
23011	51.69	2020-04-21	18:33:18	5	58960.8
22341	32.12	2020-04-29	09:07:29	5	58968.4
23233	34.59	2020-05-01	13:36:01	5	58970.6
23010	25.72	2020-07-27	11:07:30	4	59057.5
23001	25.62	2020-07-28	05:42:17	6	59058.2
23009	25.01	2020-07-28	23:57:16	6	59059.0
22340	25.62	2020-10-14	17:14:19	6	59136.7
24832	27.59	2020-10-15	05:57:17	6	59137.3
22997	26.60	2020-10-15	18:40:16	6	59137.8
24834	26.91	2020-10-16	07:35:44	5	59138.3
22342	34.50	2020-10-20	03:07:56	6	59142.1
24842	29.57	2020-10-21	01:56:20	6	59143.1
22993	24.63	2020-10-23	05:55:39	6	59145.3
22998	23.09	2020-11-01	04:40:26	5	59154.2
22999	35.58	2020-11-08	07:34:20	5	59161.3
24830	26.52	2020-11-22	07:56:09	4	59175.3
24622	24.56	2020-11-23	09:17:18	4	59176.4
24873	24.74	2020-11-24	03:01:16	4	59177.1
24874	25.72	2020-11-24	15:24:52	4	59177.6
24829	26.46	2020-11-27	14:58:09	4	59180.6
24623	24.74	2020-11-29	13:30:17	4	59182.6
24624	29.67	2020-12-09	22:23:51	4	59192.9
23002	30.66	2020-12-10	13:20:39	4	59193.6
23004	32.14	2020-12-12	01:34:32	4	59195.1
24831	30.66	2020-12-25	05:12:20	4	59208.2
24906	28.60	2020-12-25	21:09:10	4	59208.9

of confusing events happens to match the expected energy of dispersed events during spectral extraction. In these cases, ACIS order sorting will erroneously assign events from a confusing source to the extracted spectrum. Therefore, we use `CrissCross` to identify scenarios where this confusion occurs so that we can account for this during spectral fitting.

`CrissCross` is run for each observation and ultimately identifies all three sources of confusion for every source of interest (e.g., Table 2). In order to achieve this goal, `CrissCross` runs through multiple steps starting with building a source list of all detected point sources and an estimation of their brightness in terms of counts per observation. This is achieved with `wavdetect`, which identifies sources with a Mexican Hat wavelet source detection algorithm. However, `wavdetect` is not designed to be run on grating observations where HETG dispersed events are often misidentified as point sources. Nevertheless, the `wavdetect` tool still correctly identifies point sources, and we crossmatch all `wavdetect` sources to the list of known COUP sources (Feigelson et al. 2005). If a detected source is within 3″ of a COUP source, then it is recognized as a valid source. If more than one `wavdetect` source is detected within 3″ of a known COUP source, the closest source is assigned to the COUP source. The majority of cluster members are near the center of the field of view where zeroth-order events dominate (Figure 1), and thus, their detection is not affected by dispersed events. Off-axis COUP point sources were also accurately matched. The location of zeroth-order point sources and the estimated number of counts for each source provided by `wavdetect` is used to calculate the location of every dispersed spectrum in each field of view. All three primary causes of confusion are then identified for every source in Table 2. The ONC HETGS observations were carried out with ACIS-S, while the COUP project used ACIS-I. Since the ACIS-S array covers a larger area of the sky, there are 27 X-ray sources detected in the HETGS ONC observations that were outside of the field of view of the COUP. Regardless of whether or not these sources represent young stars in the ONC, we include these objects when considering the spectral confusion of the bright HETGS sources. All of these X-ray sources have 2MASS counterparts.

Point-source confusion occurs when a zeroth-order point source is detected on or near an HEG or MEG arm of an extracted source within some margin. Since the Chandra PSF increases in radius as a function of distance off-axis (i.e., distance from the optical axis or aimpoint), the margin used to initially determine whether a point source is a confuser also depends on the off-axis angle. A point source located within 3′

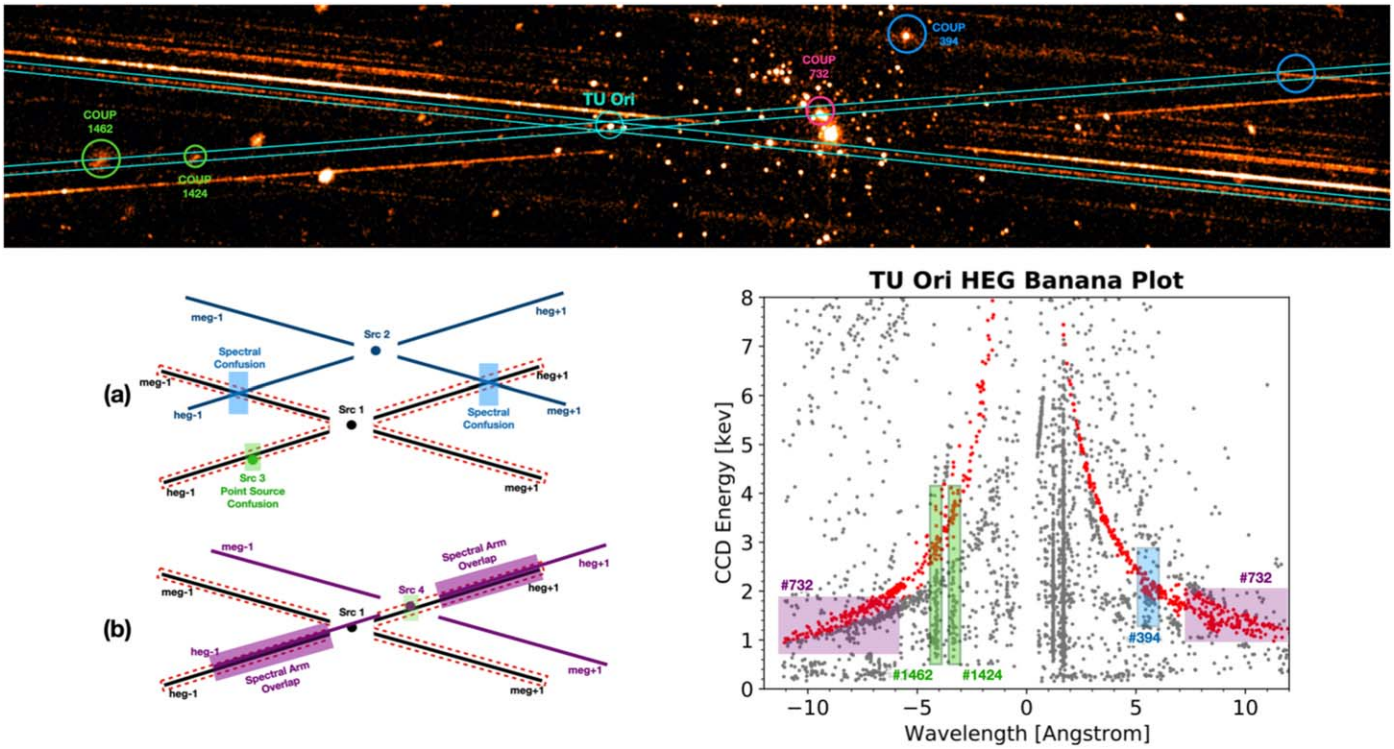

Figure 2. Top: an example HETG observation (ObsID 3) demonstrating the need to account for confusion when extracting spectra in the ONC data set. An example dispersed spectrum of TU Ori is displayed (cyan rectangle) with sources of confusion highlighted with circles (green: point source confusion, blue: spectral confusion, magenta: spectral arm overlap). Left: an illustration (not to scale) demonstrating (a) point source (green) and spectral (blue) confusion and (b) spectral arm confusion (magenta). The black X labeled Src 1 corresponds to the source intended for spectral extraction, with the red dashed box corresponding to dispersed events. Specific locations in the extracted spectra where confusion can occur are identified with colored boxes. Right: ACIS order sorting banana plot showing confused events from different sources in the field erroneously being assigned to the spectra of TU Ori. Red dots indicate events that standard `CIAO` processing assigns to the extracted source (TU Ori), while other events whose CCD-resolved energy does not match the expected wavelength of TU Ori are not included in the standard `CIAO` source extraction. Colored numbers represent the COUP number of the source causing confusion for this case. Examples where standard `CIAO` processing has the potential to erroneously include events from other sources in the extracted spectrum of TU Ori are shown as red dots within the colored boxes.

of the aimpoint is initially considered a potential confusing source if its centroid is located within 8 pixels ($\sim 4''$) of the dispersed arm in the cross-dispersion direction (perpendicular to the arm on the CCD). If a source is considered confusing, the energy and number of events within the fraction of the PSF that overlaps with the spectral arm of the extracted source is estimated. The number of zeroth-order counts in the same energy range for the source intended for spectral extraction is also determined. If the confusing source contributes more than 10% of the counts in the specific energy range where confusion occurs, then it is considered a genuine case of point source confusion.

Spectral confusion occurs when the dispersed spectrum of a confusing source intersects with the dispersed spectrum of the source intended for spectral extraction. In most cases, this type of event confusion is already removed with ACIS order sorting under standard `CIAO` processing. However, if the location where the two spectra intersect corresponds to the same energy in both spectra (i.e., the confusing events are within the order sorting energy range of the extracted spectrum), then genuine confusion will occur and the confusing events could be erroneously assigned to the extracted source's spectrum. `CrissCross` identifies these cases and determines the number of counts in both the confuser and extracted sources zeroth orders in the same energy range. After accounting for the different efficiencies between the HEG and MEG spectral arms, if the ratio of zeroth-order confuser counts to zeroth-order extracted counts is greater than 15%, it is considered a genuine source of spectral confusion.

The final primary cause of confusion in the ONC HETGS data set comes from spectral arm confusion. Cases of spectral arm confusion occur when a bright zeroth-order point source (e.g., a source bright enough to disperse many events in the first order) falls on or near the spectral arm of a source intended for extraction. Identifying potential cases of spectral arm confusion begins by identifying zeroth-order point sources with more than 50 cts that fall within a specific cross-dispersion distance of the intended source for spectral extraction. As is the case with point source confusion, we consider an off-axis angle when determining an appropriate cross-dispersion distance for potential confusion. A single on-axis source will have a cross-dispersion width of about $\sim 4''$ (8 pixels). As the PSF gets larger and farther off-axis, the cross-dispersion distance used to identify confusing sources is increased based on the off-axis locations of both the confusing and the intended source for spectral extraction.

Unlike other sources of confusion, spectral arm confusion has the potential to contaminate the entire HEG or MEG arm of the source intended for extraction. If the zeroth-order location of the two sources is close enough in the dispersion direction, many of the confusing spectral events can fall in an energy window that the extracted source is expecting (i.e., ACIS order sorting would erroneously assign events from the confused source to the extracted source). For every potential arm confusing case, `CrissCross` uses the distance between two

Table 2
HETGS First-order Master Source Table

Star	R.A.	Decl.	Primary Spec. Type	$T_{\rm eff}$ (kK)	Mass ($M_\odot$)	log(age) (yr)	COUP (#)	First Order (cts)	$f_{\rm cl}$	Fin. Exp (ks)
θ^1 Ori C	$5^{\rm h}35^{\rm m}$ 16.$^{\rm s}$46	−5°23′ 22.″8	O7V	44.6	35	⋯	809	1,033,433	1.00	2085
θ^2 Ori A	$5^{\rm h}35^{\rm m}$ 22.$^{\rm s}$90	−5°24′ 57.″8	O9.5IV	30.9	25	⋯	1232	19,573	0.85	1445
θ^1 Ori A	$5^{\rm h}35^{\rm m}$ 15.$^{\rm s}$83	−5°23′ 14.″3	B0.5Vp	28.8	15	⋯	745	71,578	0.48	1276
θ^1 Ori B	$5^{\rm h}35^{\rm m}$ 16.$^{\rm s}$14	−5°23′ 06.″8	B3V	⋯	7	⋯	778	0	0	0
θ^1 Ori E	$5^{\rm h}35^{\rm m}$ 15.$^{\rm s}$77	−5°23′ 09.″9	G2IV	14.8	2.8	⋯	732	131,865	0.67	1592
θ^1 Ori D	$5^{\rm h}35^{\rm m}$ 17.$^{\rm s}$26	−5°23′ 16.″6	B1.5Vp	32.4	16	<6.39	869	0	0	0
θ^2 Ori B	$5^{\rm h}35^{\rm m}$ 26.$^{\rm s}$40	−5°25′ 00.″8	B0.7V	29.5	15	<6.30	1360	0	0	0
MV Ori	$5^{\rm h}35^{\rm m}$ 18.$^{\rm s}$67	−5°20′ 33.″7	F8-G0	5.24	2.72	6.17	985	17,368	0.74	1189
TU Ori	$5^{\rm h}35^{\rm m}$ 20.$^{\rm s}$22	−5° 20′57.″2	F7-G2	5.90	2.43	5.55	1090	9813	0.53	1027
V2279 Ori	$5^{\rm h}35^{\rm m}$ 15.$^{\rm s}$93	−5°23′ 50.″1	G4-K5	5.24	2.37	6.12	758	16,545	0.27	1058
V348 Ori	$5^{\rm h}35^{\rm m}$ 15.$^{\rm s}$64	−5°22′ 56.″5	G8-K0	5.24	2.33	6.23	724	34,731	0.43	1236
V1399 Ori	$5^{\rm h}35^{\rm m}$ 21.$^{\rm s}$04	−5°23′ 49.″0	G8-K0	5.11	2.28	6.17	1130	32,765	0.63	1816
V1229 Ori	$5^{\rm h}35^{\rm m}$ 18.$^{\rm s}$37	−5°22′ 37.″4	G8-K0	5.24	2.22	6.14	965	28,267	0.55	1349
V2299 Ori	$5^{\rm h}35^{\rm m}$ 17.$^{\rm s}$06	−5°23′ 34.″.″2	K0-K7	5.11	2.08	6.27	855	10,640	0.23	905
LR Ori	$5^{\rm h}35^{\rm m}$ 10.$^{\rm s}$51	−5°26′ 18.″3	K0-M0	5.24	2.05	6.43	387	9549	0.73	1193
2MASS3	$5^{\rm h}35^{\rm m}$ 17.$^{\rm s}$22	−5°21′ 31.″7	K4-K7	4.68	1.97	5.56	867	7024	0.50	942
MT Ori	$5^{\rm h}35^{\rm m}$ 17.$^{\rm s}$95	−5°22′ 45.″5	K2-K4	4.58	1.99	5.39	932	150,965	0.84	1701
LU Ori	$5^{\rm h}35^{\rm m}$ 11.$^{\rm s}$50	−5°26′ 02.″4	K2-K3	4.78	1.86	6.07	430	13,386	0.77	1259
V1338 Ori	$5^{\rm h}35^{\rm m}$ 20.$^{\rm s}$17	−5°26′ 39.″12	K0-G4	5.25	1.83	6.32	1087	0	0	0
Par 1841	$5^{\rm h}35^{\rm m}$ 15.$^{\rm s}$18	−5°22′ 54.″53	K6-G4	5.25	1.83	6.74	682	0	0	0
V1333 Ori	$5^{\rm h}35^{\rm m}$ 17.$^{\rm s}$00	−5°22′ 33.″0	K5-M3	4.95	1.68	6.32	854	13,484	0.31	918
V2336 Ori	$5^{\rm h}35^{\rm m}$ 18.$^{\rm s}$70	−5°22′ 56.″8	K0-K3	4.79	1.65	6.50	993	0	0	0
Par 1842	$5^{\rm h}35^{\rm m}$ 15.$^{\rm s}$27	−5°22′ 56.″8	G7-G8	5.56	1.56	6.62	689	15,783	0.19	941
V1330 Ori	$5^{\rm h}35^{\rm m}$ 14.$^{\rm s}$90	−5°22′ 39.″2	K5-M2	4.58	1.47	5.88	670	21,357	0.41	1314
Par 1837	$5^{\rm h}35^{\rm m}$ 14.$^{\rm s}$99	−5°21′ 59.″93	K3.5	4.58	1.47	6.30	669	6956	0.54	1096
Par 1895	$5^{\rm h}35^{\rm m}$ 16.$^{\rm s}$38	−5°24′ 03.″35	K4-K7	4.00	0.91	5.59	801	5724	0.28	838
V1279 Ori	$5^{\rm h}35^{\rm m}$ 16.$^{\rm s}$76	−5°24′ 04.″3	M0.9e	4.20	0.91	5.84	828	13,683	0.64	1251
V491 Ori	$5^{\rm h}35^{\rm m}$ 20.$^{\rm s}$05	−5°21′ 05.″9	K7-M2	3.99	0.74	5.92	1071	18,586	0.78	1380
Par 1839	$5^{\rm h}35^{\rm m}$ 14.$^{\rm s}$64	−5°22′ 33.″70	K7	3.99	0.74	5.30	648	6382	0.27	877
LQ Ori	$5^{\rm h}35^{\rm m}$ 10.$^{\rm s}$73	−5°23′ 44.″7	K2	3.90	0.70	3.99	394	34,093	0.84	1617
V1326 Ori	$5^{\rm h}35^{\rm m}$ 09.$^{\rm s}$77	−5°23′ 26.″9	K4-M2	3.90	0,64	5.76	343	17,530	0.68	1402
COUP 1023	$5^{\rm h}35^{\rm m}$ 19.$^{\rm s}$21	−5°22′ 50.″7	K5-M2	4.40	0.62	6.36	1023	6119	0.39	815
V495 Ori	$5^{\rm h}35^{\rm m}$ 21.$^{\rm s}$66	−5°25′ 26.″5	M0	3.80	0.58	6.43	1161	13,126	0.83	1453
V1527 Ori	$5^{\rm h}35^{\rm m}$ 22.$^{\rm s}$55	−5°23′ 43.″7	M0	3.80	0.57	6.43	1216	0	0	0
V1228 Ori	$5^{\rm h}35^{\rm m}$ 12.$^{\rm s}$28	−5°23′ 48.″0	K1-M0	3.80	0.56	5.95	470	9440	0.36	1133
V1501 Ori	$5^{\rm h}35^{\rm m}$ 15.$^{\rm s}$55	−5°25′ 14.″15	K4-M1	3.80	0.55	4.65	718	16,384	0.87	1564
2MASS4	$5^{\rm h}35^{\rm m}$ 23.$^{\rm s}$81	−5°23′ 34.″3	M1e	3.72	0.47	6.21	1268	0	0	0
V1496 Ori	$5^{\rm h}35^{\rm m}$ 13.$^{\rm s}$80	−5°22′ 07.″02	K2e	3.43	0.39	5.16	579	6425	0.49	1040
2MASS1	$5^{\rm h}35^{\rm m}$ 09.$^{\rm s}$77	−5°21′ 28.″3	M3.5	3.31	0.28	6.52	342	13,960	0.90	1581
COUP 450	$5^{\rm h}35^{\rm m}$ 11.$^{\rm s}$80	−5°21′ 49.″3	M4.4	3.16	0.22	6.47	450	24,771	0.85	1642
Par 1936	$5^{\rm h}35^{\rm m}$ 19.$^{\rm s}$30	−5°20′ 07.″9	K2	4.95	1.4	6.78	1028	4301	0.55	959
V1230 Ori	$5^{\rm h}35^{\rm m}$ 20.$^{\rm s}$72	−5°21′ 44.″3	B1	18.6	6.4	⋯	1116	24,363	0.83	1507
COUP 662	$5^{\rm h}35^{\rm m}$ 14.$^{\rm s}$90	−5°22′ 25.″41	⋯	⋯	⋯	⋯	662	4026	0.33	750
JW 569	$5^{\rm h}35^{\rm m}$ 17.$^{\rm s}$95	−5°25′ 21.″24	M3.5	3.16	0.1	⋯	936	0	0	0
V1398 Ori	$5^{\rm h}35^{\rm m}$ 13.$^{\rm s}$45	−5°23′ 40.″43	M0	⋯	⋯	⋯	545	7068	0.43	980

zeroth orders in the dispersion direction to evaluate the boundaries in energy space within a spectrum where a standard spectral extraction would have erroneously included events from the confused source. These spectral regions are then flagged as confused and accounted for in spectral fitting (Section 2.5).

The three causes of confusion were determined for every source in Table 2 on a per-epoch basis and collated into a master table to be used in spectral cleaning (Section 2.5). The reduction and analysis of the high-resolution X-ray spectra in Table 2 from the 70 HETGS observations of the ONC represents a very large data set with tens of thousands of potential instances of confusion over all the individual spectra. Many instances of confusion were checked by eye but it is not feasible to check them all. Therefore, conservative parameter values were chosen with `CrissCross` to err on the side of removing some genuine source events in an effort to ensure confusion events are not included in our final spectral extractions. This provides a first set of quality spectra for analysis.

2.5. Spectral Cleaning Process

The spectral extraction results in standard products for data analysis for all sources over the entire exposure. This includes a PHA file containing binned spectra, and their corresponding ARFs and RMFs. We did not extract backgrounds adjacent to spectra since the *background* will be largely due to confusing sources, both zeroth orders and dispersed spectra as described

in Section 2.4. For this analysis, we combine the single source spectra (i.e., PHA files) into one merged spectrum but ignore the confused regions. To do this, we load all the spectra for a given source, then apply the confusion information, which defines the regions to be ignored in each order of each spectrum. The confusion analysis described in Section 2.4 produced a confusion table that contains all locations where cluster stars interfere with each other either via zero-order overlaps with grating arms spatially or where grating arms overlap with each other spatially *and* in PHA space. In standard analysis of a single, isolated source, the PHA is used to sort the grating orders. In a multisource confused situation, as we encounter in the ONC, PHA space also has to sort out orders from other confusing sources. The application of the information from the confusion table is straightforward for the zero-order point-source overlaps, but somewhat subjective when it comes to confusion due to spectral arm overlaps. Here, we defined a parameter, which is basically the zero-order flux ratio of the involved sources, that controls how low of an interfering overlap we allow with respect to contributing flux. The farther below unity this parameter is chosen to be, the more overlapping flux is excluded. This has to be done manually by adjusting this parameter until the HEG and MEG positive and negative first-order fluxed spectra agree within their statistical uncertainties. Here, it is mandatory that *all* four spectral arms agree. This then defines the exclusion criteria, i.e., the *ignore* ranges in each spectral histogram.

Table 2 lists the total number of counts in the added HETG first orders after that cleaning procedure was applied and an effective exposure. The effective exposure shows how much of the original 2 Ms exposure remained for each source. In theory, for bright sources, such as θ^1 Ori A, C, E, and MT Ori, there should be little arm confusion. It turned out that this was only true for θ^1 Ori C, mostly because it is so much brighter than any of the other sources. The other three sources suffered significant losses due to unfortunate observation roll angles which resulted in the situation that they confused each other. Here, θ^1 Ori E interfered with θ^1 Ori C and A. The latter source suffered the most as it overlapped with three very bright sources, θ^1 Ori C, E, and MT Ori. This situation was anticipated and minimized during observation planning by selecting more favorable roll angles. We also had over half a dozen cases where overlaps were so severe that, at this point, we could not recover any reasonable flux in the first orders. We note that the method we apply here is likely overcleaning the spectra, i.e., future refinements may improve these numbers, even recover first-order counts in those sources that have zero counts and zero effective exposures in the present analysis.

In order to compare the resulting spectra with spectral models, the models must also ignore the same regions in the responses and sum to the cleaned observed counts. The rigorous way to do this would be to zero the corresponding channel range in the response matrix. However, since the response matrices for HETG dispersed orders are nearly diagonal, and since regions are randomly distributed throughout the count spectra, it is easier to modify the ARF in the same way as the counts. We can, thus, for each order and grating type, add the counts, add the ARFs with exposure weighting, and use the RMF as is to provide a merged set of data products suitable for further analysis. These data products, i.e., the cleaned merged spectra and their corresponding ARFs and RMFs, are available to the public and can be downloaded from the Chandra archive contributed data page[12] and alternatively from Zenodo.[13]

3. Source Detection and Master Source List

3.1. Zeroth-order Source Detection

The main field of view of Figure 1 shows the merged zero-order image of the ONC as observed with the Chandra HETG. We ran `wavedetect` on that field of view and compared the resulting source list with the COUP source list (Getman et al. 2005). Some of the sources in the COUP list were not detected, even though based on their brightness during the COUP campaign, they should have been detectable. This emphasizes the extreme flux variability young stars exhibit in X-rays.

3.2. First-order Source List

We have accumulated a final master source list that emerged after all cleaning procedures. Of the 45 sources we found to be bright enough to produce good first-order spectra, which are shown in Table 2, 36 sources survived the cleaning process described in Section 2.5 with well above several 1000 first-order counts. One source, θ^1 Ori C remained with over 2 Ms exposure after cleaning and 25 sources have between 1 and 2 Ms exposures. The smallest exposure is for COUP 662 with 750 ks. 24 sources yield over 10,000 first-order counts, 11 sources have more than 5000 cts, and only two sources are below that number. Nine sources were excluded because their spectra had less than a few 100 cts left after cleaning. These sources are fainter than the rest and we anticipate that future improvements in the cleaning procedure may recover some more counts. Table 2 provides the number of the final number of counts after cleaning, the fraction of counts between the final spectra divided by the original number of counts as a figure of merit toward the cleaning process $f_{\rm cl}$. It also states the final remaining exposure after the cleaning process.

As expected, all bright sources were detected by COUP (Feigelson et al. 2005) and Table 2 provides the COUP numbers of the object as well as the coordinates as provided by COUP (Getman et al. 2005). The table also provides some physical parameters describing each source, which were collected from previous optical studies (Hillenbrand 1997; Herbig & Griffin 2006; Da Rio et al. 2010; Hillenbrand et al. 2013; Maíz Apellániz et al. 2022). In fact, the table itself is approximately sorted by modeled stellar masses, even though for some stars, we could not find model predictions.

All of the early (O and B) type stars in our sample are known to be multiple systems (see Petr et al. 1998; Preibisch et al. 1999; Grellmann et al. 2013; Karl et al. 2018, and references therein). Table 2 lists only the properties of the primary component, but a summary of the companion properties is provided in Table 3.

3.3. Gaia Distances of the ONC and Our Stellar Sample

Thanks to Gaia parallaxes, the distance to the ONC is very well known today. In a recent study (Maíz Apellániz et al. 2022) based on the Gaia DR3 data, a distance of $D = (390 \pm 2)$ pc was determined for a sample of astrometrically selected cluster members.

[12] https://cxc.harvard.edu/cda/contributedsets.html
[13] doi:10.5281/zenodo.10853416

Table 3
Multiplicity and Components of θ^1 Ori and θ^2 Ori

Star	Comp.	SpT	Mass ($M_\odot$)	Separation (au)
θ^1 Ori A—	1	B0.5Vp	15	⋯
	2		≈4	100
	3		≈2.6	0.71
θ^1 Ori B—	1	B3V	7	⋯
	2		≈4	382
	3		≈3	49
	4		≈1	248
	5		≈2	0.12
	6		≈2	5
θ^1 Ori C—	1	O7V	35	⋯
	2		9	18.1
	3		≈1	0.41
θ^1 Ori D—	1	B1.5Vp	16	⋯
	2		≈1	580
	3		≈6	0.77
θ^1 Ori E—	1	G2IV	2.8	⋯
	2	G0IV-G5III	2.8	0.09
θ^2 Ori A—	1	O9.5IV	≃25	⋯
	2		≈10	0.42
	3		≈10	157
θ^2 Ori B—	1	B0.7V	15	⋯
	2		≈1.6	40

References. Preibisch et al. (1999); Kraus et al. (2009); Grellmann et al. (2013); Karl et al. (2018); Maíz Apellániz et al. (2022).

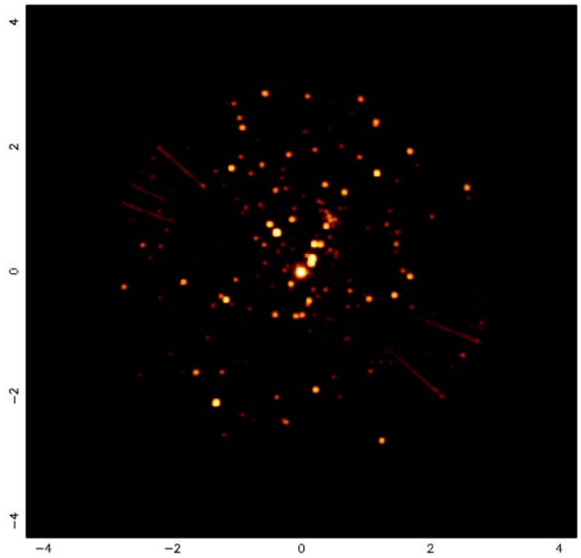

Figure 3. Example image of the ONC for approximately 3′ around θ^1 Ori C. This image represents 10% of the exposure time on this field during the 2018–2019 campaign, whereas the associated video includes all of the exposure time on this field. The video is composed of frames with 1 ks of the exposure time in sequential order, organized into a movie to highlight the remarkable short-term variability of the sources in this region. The video runs 16 minutes, 40 s at normal speed. In many cases, a source varies from bright to not detectable in the space of 1 frame (1 ks).
(An animation of this figure is available.)

Although it is highly likely that the X-ray selected stars in our Master Source List are ONC members, the X-ray detection alone does not immediately prove that this star is actually a young star in the ONC; there may be some level of contamination by foreground and background objects.

In order to check this, we obtained the parallaxes for the stars in our Master Source List from the Gaia DR3 archive. Parallaxes were found for 43 of the 45 stars in our Master Source List; the two exceptions are COUP 450 and COUP 662. We performed the bias correction of the parallaxes with the algorithm described in Lindegren et al. (2021).

All parallaxes are approximately in the expected range for ONC members around $\varpi \approx 2.5$ mas, and there are no immediately obvious foreground or background objects in the sample. However, the parallaxes show (of course) some scatter, and there are four stars (V2299 Ori, V1279 Ori, LQ Ori, and Par 1936) for which the 3σ uncertainty range for their parallax (i.e., $\varpi \pm 3\,\sigma_\varpi$) does not include the expected value, which, in principle, qualifies them as *outlier candidates*. However, in all four cases, the renormalized unit weight error (RUWE) associated with the Gaia data of these stars is high (>1.4). The RUWE value is a goodness-of-fit statistic describing the quality of the astrometric solution (see Lindegren et al. 2021), and RUWE values above 1.4 indicate low reliability of the astrometric parameters (Fabricius et al. 2021).

We determined the most likely distance to the sample of stars in our Master Source List with a Bayesian inference algorithm, employing the program `Kalkayotl` (Olivares et al. 2020). `Kalkayotl` is a free and open code that uses a Bayesian hierarchical model to obtain samples of the posterior distribution of the cluster mean distance by means of a Markov Chain Monte Carlo technique implemented in PyMC3. `Kalkayotl` also takes the parallax spatial correlations into account, which improves the credibility of the results, and allows to derive trustworthy estimates of cluster distances up to about 5 kpc from Gaia data (Olivares et al. 2020).

We used `Kalkayotl` version 1.1. For the prior, we used the implemented Gaussian model with a mean distance of $D_{\rm prior} = (390 \pm 10)$ pc and a cluster scale of $S_{\rm prior} = 10$ pc. The calculations were done in distance space, and the reported uncertainties for the inferred mean distances are the central 68.3% quantiles (corresponding to the "$\pm 1\sigma$ range" for a Gaussian distribution).

For the complete sample of 43 stars with parallaxes, we obtained a distance of 396.5 pc with an uncertainty range of [391.8, 401.2] pc. Excluding the abovementioned four *outlier candidates*, the result changes only very slightly to 395.9 pc with an uncertainty range of [392.9, 398.9] pc. These distance values for our sample are well consistent with the above-mentioned distance determination for the ONC.

4. Global HETG Properties

4.1. Zeroth-order Light Curves

The field of the Orion VLP observations includes a wealth of sources that vary in brightness with time. Many of the sources are late-type stars that can flare. Figure 3 shows a video that gives a full appreciation of variability in this field by watching the zeroth orders of the spectra as they change with time. The video was created from the merged evt2 event file of all 70 ObsIDs, split equally into 1000 frames. Therefore, each frame is a subsample of the total exposure time.

We have examined the light curve of the zeroth order of each source listed in Table 2, searching for variability. The light curves were binned into 1 ks bins for each ObsID individually, then concatenated for each source. Sources for which the zeroth

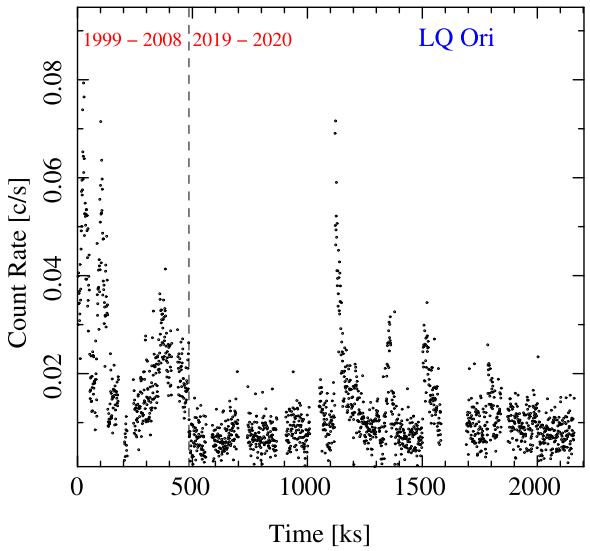

Figure 4. Concatenated light curve for LQ Ori observations, each in 1 ks bins. Time on the *x*-axis is the cumulative observing time since the beginning of the first observation. Data for ObsIDs where confusion affects the zeroth-order count rate have been eliminated in the plot.

order was confused by an overlaying spectral arm of another source in an ObsID, as determined by method described in Section 2.4, were eliminated from the variability analysis.

We investigated the variability of the zeroth order of the spectrum for each of the 45 sources using the Gregory–Lorado variability index. The variability index is determined using the algorithm of Gregory & Loredo (1992), as implemented in `CIAO` as `glvary`, and is based on the probability that the count rate of the source is not constant during the observation, using a comparison of binned event arrival times. This index is normally used only within an individual observation, but can also be used for merged data if the good time intervals are properly handled. According to Rots (2012), if the source has a variability index of 0–3, it is not considered variable within the observation. A variability index of 8 or above is definitely variable. To examine the variability of each source, a merged file of all non-confused observations was created (see Table 1 for a list of observations). `glvary` was used to evaluate the variability index for this set of non-confused observations for each source. We find that all sources are definitely variable with a variability index of 9–10, except for COUP 1023, which is possibly variable, and θ Ori D and V1527 Ori, which are not variable. An example of the zeroth-order light curves produced by the merged observation files is shown in Figure 4. The remainder of the zeroth-order light curves appear in Appendix A. The time gaps between the individual observations have been eliminated in these plots, and the light curves display the data as if they were one long continuous observation for each source. Data for confused zeroth orders are not included in the light curves.

The analysis of flares in later-type stars is an important component of the Orion VLP program. The ultimate goal is to analyze the high-resolution spectra near the times of flares to obtain detailed information about the spectral parameters both before and after the flares. A follow-on paper will identify the timing and other parameters of flares using the zeroth-order light curves presented here.

4.2. HETG First-order Spectra and Background

The sample of 36 sources that passed the cleaning process contains four massive ($>6\,M_\odot$) stars, about a dozen intermediate-mass ($\sim$2–3 $M_\odot$) stars, and about 20 low-mass ($<2\,M_\odot$) stars (see Table 2). The modeling of the spectra and the X-ray line emission is done in various steps. One item is a selective bandpass. The bright sources, as observed in the early phases of the Chandra mission, also have low absorption and provide significant flux above 16 Å. Observations in cycles later than Chandra Cycle 16 have too much contaminant absorption to allow for much flux above 16 Å. Thus, we allow a wider bandpass for bright sources analyzed in the early Chandra Cycles up to 22 Å, while limiting the bandpass for sources otherwise to 16 Å. The model spectra apply the Astrophysical Database Emission Database (APED) to fit collisionally ionized emissions to the spectra. The number of temperature components mostly depends on the need to cover the available wavelength range but also depends on the strength of the recorded X-ray continuum. As for the fitting procedure, we applied a number of APED temperature components plus background. All models have thermal line broadening applied and are folded forward through the instrument responses, then fitted to the data applying appropriate statistics.

Most of the stars in the sample are fainter than a few 10^{-13} erg cm^{-2} s^{-1} and thus require the inclusion of an X-ray background, which becomes significant at soft X-rays. This background consists mainly of an HETG/ACIS-S instrumental component[14] with some contribution of a flat diffuse stellar background from weak off-axis sources from the outer regions of the ONC cluster. Given that we have so many roll angles involved in the available 70 observations, this background should be fairly isotropic for all sources. The sample contains over half a dozen of absorbed sources where we can directly determine this background contribution. Figure 5 shows the example of COUP 450. It is heavily absorbed, and the hard X-ray bandpass below 9 Å is fitted by a single APED temperature function, while the soft part directly shows this background. It is a power law of photon index 6.5 with a normalization of 6.068×10^{-5} photons cm^{-2} s^{-1}. We tested this function with half a dozen absorbed sources with power-law parameters agreeing within 5%. We then added this power law to every spectral fit procedure. This rising tail beyond 13 Å is well predicted by the empirically measured instrumental background.

4.3. Massive Stars

There are four massive stars in the sample: the two most massive are θ^1 Ori C (O7 V) and θ^2 Ori A (O9.5 IV), plus two less massive stars θ^1 Ori A and V1230 Ori. Even though all of these stars are bright with respect to the HETG background, we include this background in all the fits. Except for V1230 Ori, some early Chandra HETG results have been published before on all the other massive stars (Schulz et al. 2000, 2003; Gagné et al. 2005; Mitschang et al. 2011). Here, we assess how the new 2.2 Ms data can serve to provide new insights.

[14] For details, see the Chandra Proposers' Observatory Guide Section 8.2.3 (https://cxc.harvard.edu/proposer/POG/html/chap8.html#tth_sEc8.2.3) and memo referenced therein.

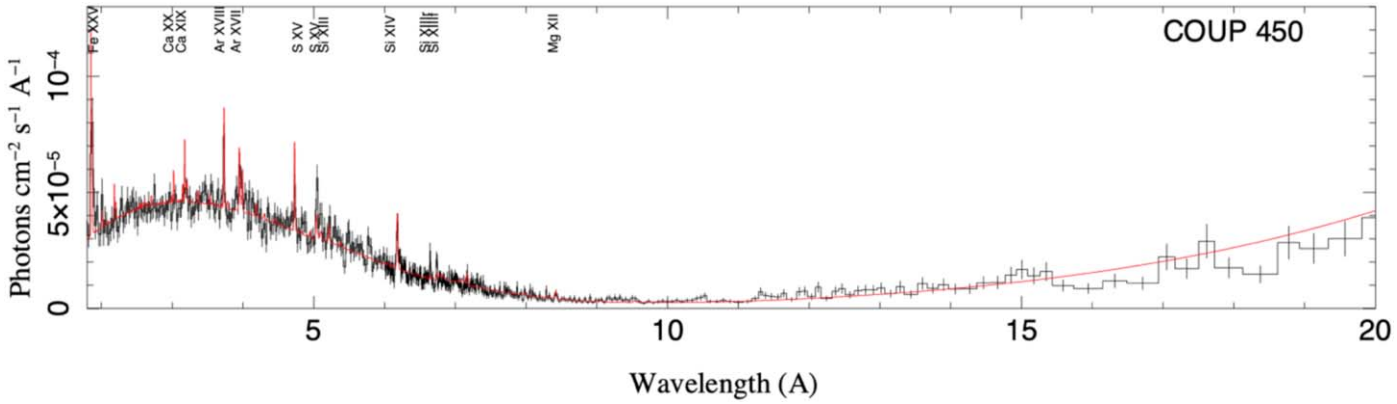

Figure 5. Absorbed one-component plasma fit with a model background for COUP 450. The background has a power-law shape and becomes noticeable above 10 Å and dominant above 16 Å; it is primarily due to local instrumental background.

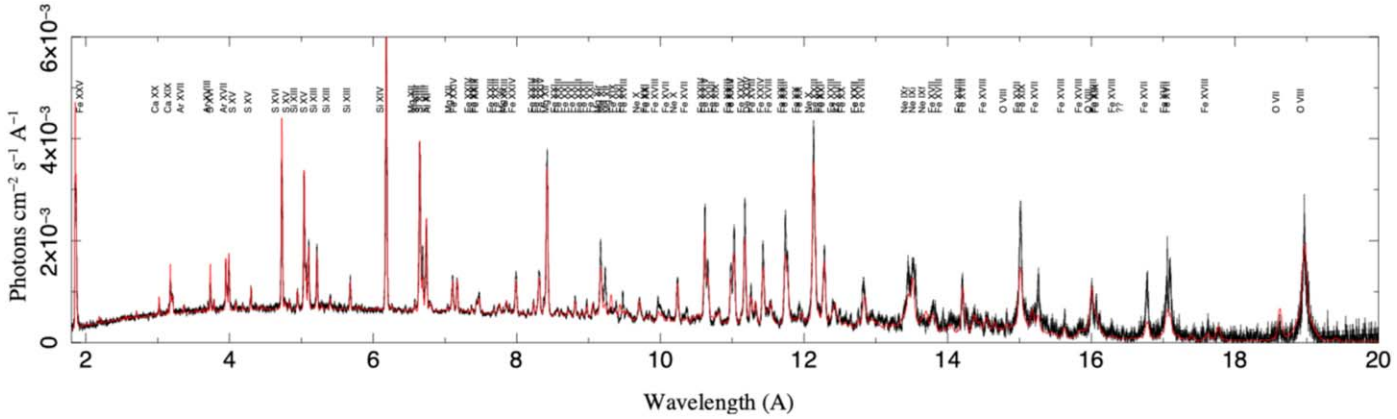

Figure 6. The broadband 2.1 Ms spectrum of θ^1 Ori C with line labels. The spectrum shows over 100 detected lines at high S/N.

4.3.1. θ^1 Ori C

The most massive component of the Trapezium cluster is the triple system θ^1 Ori C, comprised of a $\sim 33\,M_\odot$ oblique magnetic rotator θ^1 Ori C1, a $\sim 1\,M_\odot$ star C3 at only ≈0.04 au (GRAVITY Collaboration et al. 2018, and references therein), and a $\sim 10\,M_\odot$ star C2 at 16.7 au, with an orbital period of 11.26 yr (Rzaev et al. 2021).

The cleaning procedure left about 95% of the exposure for θ^1 Ori C intact, yielding a total exposure time of 2.085 Ms in 68 ObsIDs. The X-ray source is very bright with an average unabsorbed 0.5–8.0 keV X-ray flux of 4.0×10^{-11} erg s^{-1} cm^{-2}, and an average X-ray luminosity $L_X \approx 7.2 \times 10^{32}$ erg s^{-1} at 395.5 pc. The high signal-to-noise ratio (S/N) HEG and MEG spectra were analyzed using a bin size as low as 0.005 Å over the 1.65–23 Å bandpass. While still very good, count statistics decline toward larger wavelengths due to interstellar absorption, and the worsening low-energy response of the ACIS-S detector. In fact, including data sets obtained after 2007 does not improve S/N above 16 Å. Figure 6 shows the combined, first-order HEG/MEG spectrum of θ^1 Ori C, exhibiting hundreds of X-ray lines in over 70 individual line complexes.

Each data bin of the spectrum of θ^1 Ori C has sufficient counts to allow for the application of Gaussian statistics with a χ^2 minimization process. We performed a fit using a multi-APED temperature model, which was successfully used in previous analyses by Schulz et al. (2003) and Gagné et al. (2005); however, on only about 10% of the exposure and selected orbital phases. The fit here involved five APED temperatures and resulted in a reduced χ^2_ν of 2.97. This fit is shown in Figure 6. While the fit appears good with respect to the continuum, the χ^2_ν shows it is not, as there are significant residuals with respect to the line fits. These residuals require a more detailed modeling approach, which has to involve more realistic line profiles. A detailed line-by-line analysis of the phase-resolved X-ray spectra will be presented by M. Gagné et al. (2024, in preparation). In addition, numerical 3D modeling of the magnetically confined wind shocks will be presented by S. Subramanian et al. (2024, in preparation). We also took a look at the actual line widths across the bandpass. For this, we restrict the analysis to fit generic Gaussian line profiles to selected bright lines in order to determine the order of magnitude of the velocity broadening in the resolved lines. We find that the lines are resolved with very moderate broadening of about 300 km s^{-1}. Specifically, we find 369 ± 16 km s^{-1} for Ne X, 279 ± 8 km s^{-1} for Mg XII, 326 ± 8 km s^{-1} for Si XIV, 381 ± 26 km s^{-1} for S XVI, and 318 ± 52 for Ar XVIII. The consistency of these values over a large wavelength range, as well as the small uncertainties, are a reflection of the superb properties of this data set.

The high significance in the emission lines in the first order of θ^1 Ori C allows the analysis of the spectral properties at the highest possible spectral resolution with nearly perfect statistics throughout the entire wave band between 1.7 and 23 Å. One example where these conditions benefit this analysis is the He-like triplets in this bandpass. Figure 7 on the left side shows the triplets from Mg, Si, S, Ar, Ca, and Fe at no data binning. The

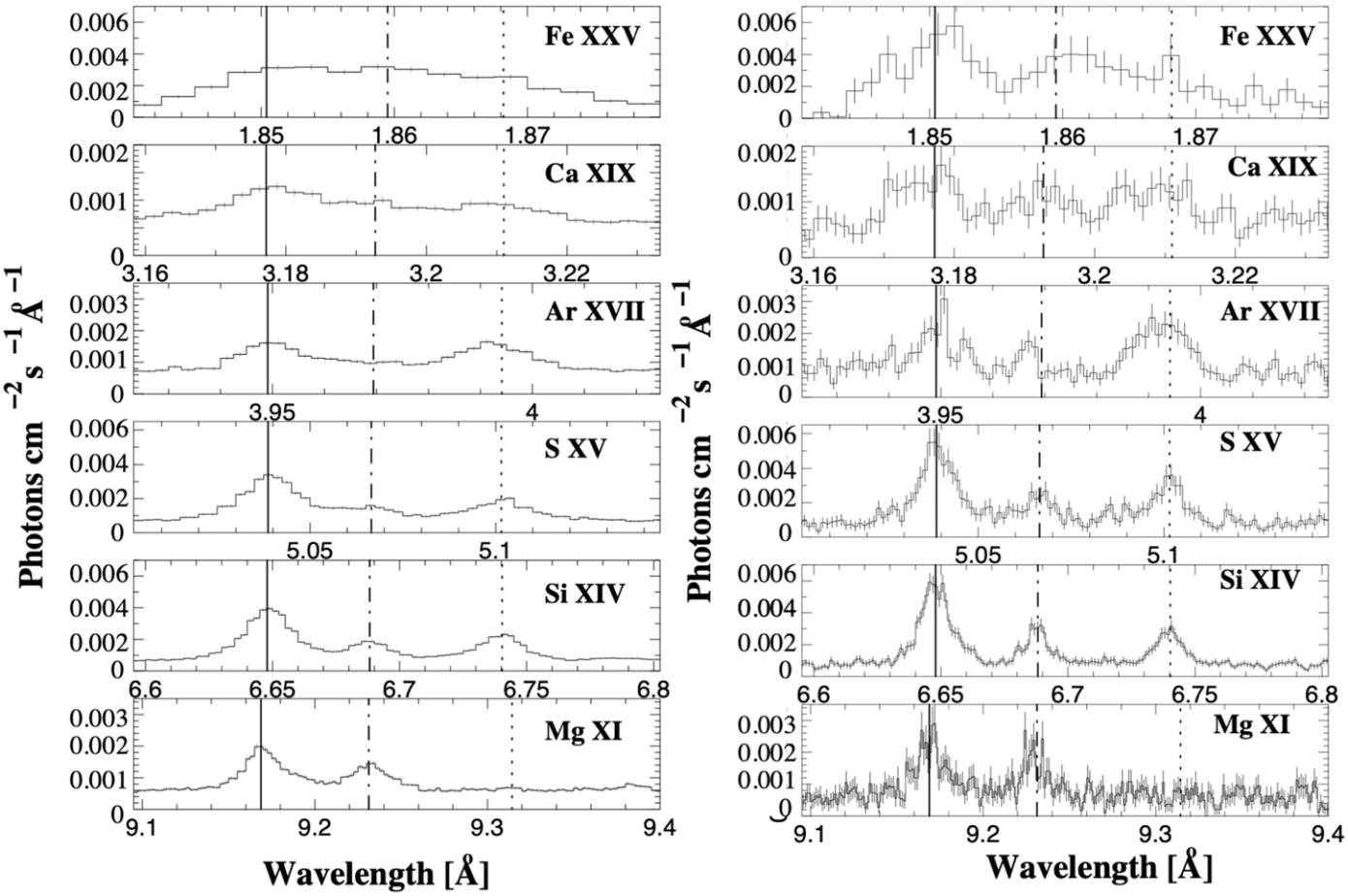

Figure 7. Here, we show He-like triplets of Mg, Si, S, Ar, Ca, and Fe in various orders for θ^1 Ori C. On the left are the triplets in first order, on the right the ones in higher orders, MEG third and HEG second orders. While the first orders provide high S/N power, the significantly higher resolving power of the higher grating orders provides much more details.

statistical 1σerrors are plotted as well but are so small that they are not visible. Previous HETG studies of the source (Schulz et al. 2000, 2003; Gagné et al. 2005) showed that the lines are well resolved with an FWHM of a few hundred kilometers per second.

The combination of high-resolution and good count statistics should prove invaluable for magnetic wind shock model analysis. However, at first-order resolution, the spectral details of the triplets start to fade past Si, i.e., the line components of higher Z triplets are not fully resolved. Here, this long exposure allows the utilization of the higher orders of the transmission gratings, specifically the MEG third and HEG second orders, which each feature nearly 10% of the first-order efficiency. Figure 7 on the right shows He-like triplets at this higher resolution. The 1σ statistical error bars are now clearly visible due to the reduced efficiency of the higher orders. However, the main triplet components are now resolved up to Ca and partially at Fe. The resolving power at Mg XI is now 1480, at Si XIII is 1000, at s XV is 820, at Ar XVII is 640, at Ca XIX is 515, and at Fe almost 310, which are the highest resolving powers in He triplets to date. Resolving He-like triplets is a very powerful tool for analysis. In the case of massive stars such as θ^1 Ori C He-like line triplet ratios are sensitive tracers of where these lines originated in the particular wind geometry. The higher Z elements we can resolve the deeper into the wind geometry we can trace. Low-Z triplets are also powerful diagnostics for accretion, higher Z can determine levels of UV exposure in stars, which is generally difficult to measure in the ONC.

4.3.2. Other Massive Stars

The three other massive stars in the sample are θ^1 Ori A, θ^2 Ori A, and V1230 Ori (see Appendix B for the spectra). For the latter two stars, the cleaning procedure leaves about 1.5 Ms of remaining exposure, while for θ^1 Ori A, the exposure is 1.2 Ms. This lower exposure is caused by the combination of this star being very close to θ^1 Ori C and a period of an unfortunate roll angle of the telescope, which caused more confusion of the two stars. In both cases, we harvest several 10^4 cts in the bandpass between 1.7 and 20 Å.

There are three more massive stars in the sample for which we could not harvest valid counts in the HETG first orders. The most prominent example is θ^1 Ori D, which is optically supposed to be very close to θ^1 Ori A, but not only do we have a large amount of confusion with other Trapezium stars, the star appears to be also very dim in X-rays, i.e., it is hardly detected even in the zeroth order. The similarity of these stars is striking, as their massive components have very similar mass, and both stars have two low- and intermediate-mass companions (see Table 3). The absence of X-ray detection can have two reasons: one is that its spectrum is very soft and suffers

from ACIS filter absorption, and another is that it is inherently X-ray weak. Both explanations are at odds with the appearance of θ^1 Ori A. Specifically, the fact that θ^1 Ori D has lower mass companions but no significant coronal emissions are detected is quite puzzling.

The other massive stars are θ^1 Ori B and θ^2 Ori B. According to Table 3, θ^1 Ori B is a cluster of at least six stars, mostly of intermediate mass. The cluster is detected in zeroth order but we do not have HETG first-order spectra. The same is true for θ^2 Ori B, which is well detected in zeroth order but no significant emissions could be recovered in HETG first order.

4.4. Intermediate- and Low-mass Stars

There are 11 stars of masses between 1.5 and 3 $M_\odot$ in the sample, which we designate as intermediate-mass stars, and 20 stars below 1.5 $M_\odot$, which we designate as low-mass stars (see Appendix B for the spectra). The mass designation is somewhat arbitrary but helps in the discussion of their properties. In the analysis, we treat them similarly to coronal sources and apply the same model to their data. This model consists of the standard soft background, column density, and two APED temperature components. The spectra have a large range in terms of statistical quality from very low to very high levels. Consequently, for all spectral fits, we use the Cash statistical concept (Cash 1979) that allows for properly treating data bins with low statistics by the use of a maximum likelihood ratio test. We dynamically binned the spectra to make sure we preserve maximum spectral resolution and have nonzero count data bins. In ISIS, we can then fit multiple APED functions with common abundance and column density values. We conducted the model fits in two steps. In a first step, we fit the spectra with all parameters free. This fit should already generate an acceptably reduced Cash statistic C_ν. However, in this overview analysis, we are not interested in all the details, and we fixed the APED abundance values to the fit result and in a second step, we computed 90% confidence limits for the absorption column $N_{\rm H}$, the involved temperatures kT_i, where i is the APED component index, and the emission measures EM_i of each component. This second step improves the Cash statistic by roughly 10%. More detailed analyses involving abundances should be done in follow-up studies within the framework of a differential emission measure analysis as described in Huenemoerder et al. (2003). We also kept the turbulent velocity v_t (in a Gaussian line profile with the width defined by $\sigma = \sqrt{\frac{2kT}{Am_h} + v_t^2}$, where k is the Boltzmann constant, T is the temperature of the component, A is the atomic number and m_h is the hydrogen mass) free to be fitted but after prescreening of all the data we constrained them to values between 100 and 500 km s^{-1} for the broadband fit, which helped stabilize the fit procedure.

In order to further characterize the actual line widths, we performed individual line fits on the Ne X and Si XIV lines in all sources where they were detected. We simply applied Gaussian functions to determine the line widths. The resulting velocities were converted from the σ width of the Gaussian line and are therefore slightly different from the APED global turbulent velocities. The final results of these fits are shown in Table 4. The broadband fits produced Cash statistics between 0.95 and 1.51, which are also listed in Table 4.

4.4.1. Surface Flux

The global fits result in X-ray fluxes of a few 10^{-13} erg cm^{-2} s^{-1} for all sources except MT Ori, which is an order of magnitude brighter. In order to determine what we call surface flux we calculate the source luminosity from the measured unabsorbed flux and divide by the surface area of the star. The radius of each star is calculated from the bolometric luminosity and the effective surface temperature, which are measured quantities and listed in the standard COUP tables.

In Figure 8, we plot the surface flux versus the age of the cluster source as listed in Table 2. These ages are also taken from the COUP tables, and even though not very well known, they allow global order of magnitude comparisons. The COUP radii are also subject to systematical uncertainties and we added a 10% contribution to the uncertainty of the surface flux. The plot shows that similar age stars have similar surface fluxes. There may be a possible trend of increasing (coronal) X-ray surface brightness with PMS age. Such a trend would seem to be consistent with studies of the evolutionary behavior of TTS X-ray emission dating back to Kastner et al. (1997) in the TW Hydra Association. There are two exceptions. V495 Ori exhibited a giant flare that lasted for a week; V491 Ori is a highly absorbed persistent source that will need special attention.

4.4.2. Absorption Column Densities

The global fits resulted in column densities $N_{\rm H}$ between a few times 10^{21} cm^{-2} and a few times 10^{22} cm^{-2}. The largest column was observed in COUP 450 with 1.3×10^{22} cm^{-2}. LQ Ori exhibits the lowest column consistent with a value below 10^{20} cm^{-2}. The column density toward the ONC is estimated to be $\sim 2.3 \times 10^{21}$ cm^{-2} (see the discussion in Schulz et al. 2015), which implies most of the excess absorption observed is likely intrinsic to the stellar systems. In Figure 9, we plot the measured X-ray absorption column versus the optical extinction.

The figure also shows other young stars from the literature for comparison. The sample of Günther & Schmitt (2008) concentrates on stars that are observed with high-resolution X-ray spectroscopy, similar to our sample from the ONC. The figure also displays two stars where the absorbing column density and the optical extinction have been observed to change with time, in particular in TWA 30A (Principe et al. 2016) and AA Tau (Grosso et al. 2007; Schneider et al. 2015). Green lines indicate $N_{\rm H}/A_V$ ratios from the interstellar medium (ISM) and two star-forming regions from Vuong et al. (2003); for the ONC those authors have only a very small sample with large uncertainties that appears compatible with the ISM.

To provide an independent means of estimating $N_{\rm H}$, we compared the flux in the Ne X alpha line with the flux in the Ne X beta line. The Ne X lines are relatively strong in the spectra of our sources and the wavelength separation of the alpha and beta lines is adequate to estimate $N_{\rm H}$. A two-temperature APED model was used for the continuum in each case and the emission lines were fit with Gaussian profiles. The ratio was used to interpolate the $N_{\rm H}$ transmission curves. The Ne-based $N_{\rm H}$ values are consistent with the ones from the APED fits.

Table 4
HETG Spectral Parameters of Two-temperature APED Fits

Star	N_H (1)	T_1 (2)	T_2 (2)	EM_1 (3)	EM_2 (3)	v_{Ne} (4)	v_{Si} (4)	f_x (5)	L_x (6)	C_ν
θ^1 Ori E	$1.7^{0.1}_{0.1}$	$12.98^{0.31}_{0.75}$	$40.62^{0.80}_{1.40}$	$2.04^{0.21}_{0.19}$	$8.05^{0.30}_{0.15}$	239^{34}_{34}	247^{34}_{35}	$53.8^{0.3}_{0.3}$	13.7	1.19
MV Ori	$10.10^{0.56}_{0.55}$	$13.81^{0.65}_{0.67}$	$90.00^{0.00}_{19.17}$	$2.25^{0.17}_{0.05}$	$0.72^{0.11}_{0.04}$	153^{96}_{227}	986^{202}_{61}	$4.6^{4.9}_{4.4}$	1.03	1.15
TU Ori	$9.20^{1.50}_{0.43}$	$15.67^{2.27}_{1.62}$	$69.09^{13.91}_{16.47}$	$1.04^{0.16}_{0.18}$	$0.56^{0.16}_{0.15}$	319^{410}_{220}	646^{484}_{597}	$2.6^{2.7}_{2.4}$	0.56	1.22
V2279 Ori	$5.43^{0.49}_{0.50}$	$9.18^{1.09}_{1.02}$	$45.61^{3.52}_{3.38}$	$0.93^{0.17}_{0.16}$	$1.50^{0.10}_{0.09}$	115^{269}_{115}	374^{257}_{167}	$4.9^{5.1}_{4.7}$	1.03	1.16
V348 Ori	$2.55^{0.25}_{0.23}$	$10.27^{0.70}_{0.71}$	$41.10^{1.66}_{1.53}$	$0.61^{0.10}_{0.09}$	$2.80^{0.08}_{0.08}$	209^{24}_{95}	258^{98}_{258}	$9.4^{9.9}_{8.9}$	1.78	1.15
V1229 Ori	$2.76^{0.28}_{0.28}$	$9.61^{0.78}_{1.19}$	$35.15^{1.31}_{1.53}$	$0.56^{0.08}_{0.09}$	$2.47^{0.07}_{0.12}$	153^{58}_{123}	679^{455}_{380}	$5.7^{6.0}_{5.5}$	1.12	1.17
V1399 Ori	$3.14^{0.36}_{0.24}$	$9.70^{0.73}_{0.76}$	$31.33^{1.16}_{1.19}$	$0.62^{0.12}_{0.09}$	$2.20^{0.09}_{0.08}$	257^{64}_{50}	268^{121}_{189}	$7.3^{7.7}_{7.0}$	1.40	1.12
V2299 Ori	$10.58^{0.84}_{0.73}$	$16.83^{2.96}_{2.71}$	$57.82^{19.51}_{10.68}$	$0.81^{0.18}_{0.55}$	$1.23^{0.45}_{0.17}$	219^{85}_{103}	218^{267}_{218}	$4.4^{4.6}_{4.2}$	0.94	1.20
LR Ori	$4.09^{0.82}_{0.74}$	$12.00^{0.87}_{1.55}$	$60.00^{11.00}_{10.53}$	$0.57^{0.13}_{0.14}$	$0.51^{0.25}_{0.03}$	213^{112}_{99}	179^{221}_{179}	$1.9^{2.0}_{1.8}$	0.37	1.28
2MASS3	$5.10^{0.84}_{0.80}$	$14.46^{1.11}_{1.32}$	$74.60^{15.40}_{17.00}$	$0.36^{0.40}_{0.03}$	$0.57^{0.09}_{0.09}$	153^{122}_{50}	50^{112}_{373}	$1.6^{1.7}_{1.5}$	0.37	1.19
MT Ori	$3.38^{0.12}_{0.11}$	$12.35^{0.78}_{0.64}$	$40.95^{0.96}_{8.17}$	$1.37^{0.22}_{0.17}$	$9.96^{0.17}_{0.22}$	195^{27}_{24}	289^{58}_{89}	$34.5^{0.8}_{1.7}$	6.73	1.14
LU Ori	$4.45^{0.63}_{0.64}$	$10.96^{0.49}_{0.48}$	$45.35^{4.58}_{3.97}$	$0.68^{0.15}_{0.14}$	$0.77^{0.06}_{0.06}$	322^{87}_{134}	470^{213}_{181}	$2.6^{2.7}_{2.4}$	0.56	1.23
V1333 Ori	$9.29^{0.58}_{0.60}$	$12.04^{0.61}_{0.75}$	$30.39^{2.57}_{2.60}$	$1.52^{0.25}_{0.27}$	$1.30^{0.20}_{0.15}$	222^{87}_{208}	636^{635}_{260}	$3.3^{3.5}_{3.2}$	0.65	1.32
Par 1842	$1.77^{0.43}_{0.37}$	$10.82^{0.93}_{1.07}$	$36.39^{2.14}_{2.19}$	$0.45^{0.11}_{0.10}$	$1.52^{0.09}_{0.08}$	216^{31}_{138}	556^{276}_{341}	$4.3^{4.5}_{4.1}$	0.84	1.17
V1330 Ori	$4.95^{0.45}_{0.40}$	$10.46^{0.74}_{0.47}$	$43.05^{3.08}_{4.95}$	$0.65^{0.13}_{0.11}$	$1.57^{0.07}_{0.08}$	152^{176}_{108}	254^{124}_{253}	$5.3^{5.6}_{5.0}$	1.03	1.14
Par 1837	$5.45^{0.37}_{0.84}$	$7.22^{1.44}_{1.49}$	$45.03^{4.66}_{5.42}$	$0.35^{0.21}_{0.09}$	$0.52^{0.06}_{0.04}$	321^{140}_{138}	597^{288}_{326}	$1.5^{1.6}_{1.4}$	0.28	1.34
Par 1895	$0.05^{0.27}_{0.04}$	$13.13^{1.93}_{1.31}$	$64.33^{15.71}_{9.72}$	$0.18^{0.05}_{0.04}$	$0.39^{0.04}_{0.05}$	318^{290}_{156}	253^{99}_{89}	$1.5^{1.5}_{1.4}$	0.28	0.95
V1279 Ori	$2.02^{0.58}_{0.40}$	$9.58^{0.92}_{1.08}$	$38.34^{2.67}_{2.52}$	$0.26^{0.10}_{0.07}$	$0.92^{0.05}_{0.07}$	279^{55}_{132}	247^{101}_{199}	$2.7^{2.8}_{2.5}$	0.47	1.20
V491 Ori	$16.21^{0.91}_{0.50}$	…	$43.40^{2.23}_{3.08}$	…	$2.69^{0.06}_{0.10}$	…	400^{358}_{220}	$7.7^{8.1}_{7.3}$	1.68	1.28
Par 1839	$2.99^{0.86}_{0.84}$	$11.67^{1.00}_{1.22}$	$81.22^{8.78}_{11.71}$	$0.48^{0.11}_{0.11}$	$0.43^{0.06}_{0.03}$	269^{88}_{164}	278^{200}_{277}	$1.9^{2.0}_{1.8}$	0.37	1.25
LQ Ori	$0.29^{0.20}_{0.23}$	$10.52^{0.36}_{0.31}$	$34.28^{2.16}_{1.32}$	$0.68^{0.11}_{0.07}$	$1.89^{0.15}_{0.30}$	213^{31}_{29}	221^{160}_{220}	$5.0^{5.3}_{4.8}$	0.94	1.16
V1326 Ori	$3.19^{0.41}_{0.44}$	$6.04^{0.55}_{0.50}$	$29.46^{1.56}_{1.21}$	$0.98^{0.21}_{0.18}$	$1.27^{0.06}_{0.06}$	191^{39}_{59}	301^{188}_{194}	$2.7^{2.8}_{2.6}$	0.56	1.51
COUP 1023	$5.56^{1.34}_{1.13}$	$18.96^{3.09}_{2.95}$	$78.00^{12.00}_{14.96}$	$0.60^{0.13}_{0.13}$	$0.28^{0.11}_{0.04}$	86^{83}_{78}	243^{193}_{145}	$1.7^{1.8}_{1.6}$	0.37	1.29
V495 Ori	$5.24^{0.72}_{0.69}$	$11.61^{1.47}_{1.01}$	$69.02^{14.58}_{9.43}$	$0.51^{0.12}_{0.11}$	$0.66^{0.06}_{0.07}$	257^{127}_{133}	307^{165}_{143}	$3.0^{3.2}_{2.9}$	0.65	1.26
V1228 Ori	$3.04^{0.80}_{1.54}$	$9.18^{0.78}_{0.65}$	$37.33^{5.33}_{2.67}$	$0.48^{0.17}_{0.10}$	$0.62^{0.05}_{0.08}$	135^{74}_{74}	359^{50}_{354}	$1.7^{1.8}_{1.6}$	0.37	1.30
V1501 Ori	$3.41^{0.82}_{0.69}$	$12.19^{0.99}_{1.29}$	$42.42^{4.09}_{5.42}$	$0.59^{0.18}_{0.15}$	$0.79^{0.11}_{0.07}$	301^{105}_{97}	384^{180}_{307}	$2.5^{2.7}_{2.4}$	0.56	1.31
V1496 Ori	$3.27^{0.83}_{0.84}$	$13.00^{2.11}_{1.44}$	$65.90^{18.16}_{10.35}$	$0.27^{0.09}_{0.07}$	$0.41^{0.05}_{0.05}$	210^{556}_{186}	36^{286}_{31}	$1.6^{1.7}_{1.6}$	0.37	1.29
2MASS1	$14.49^{0.82}_{0.82}$	$12.07^{1.61}_{1.32}$	$47.93^{9.85}_{6.32}$	$1.27^{0.27}_{0.28}$	$1.08^{0.18}_{0.18}$	…	770^{246}_{293}	$3.6^{3.8}_{3.4}$	0.84	1.25
COUP 450	$30.95^{0.78}_{0.78}$	…	$34.92^{1.55}_{1.34}$	…	$5.58^{0.12}_{0.26}$	…	460^{603}_{302}	$11.2^{0.5}_{0.6}$	3.09	1.15
Par 1936	$16.88^{1.94}_{1.76}$	$13.28^{1.54}_{1.42}$	$83.00^{7.00}_{7.05}$	$0.80^{0.21}_{0.16}$	$0.26^{0.03}_{0.02}$	…	356^{1089}_{356}	$1.3^{1.4}_{1.2}$	0.28	1.32
COUP 662	$21.52^{1.66}_{1.60}$	…	$89.00^{1.00}_{1.00}$	$0.00^{0.00}_{0.00}$	$0.62^{0.02}_{0.02}$	…	364^{729}_{359}	$2.6^{2.7}_{2.5}$	0.56	1.37
V1398 Ori	$5.01^{1.05}_{1.24}$	$12.89^{1.31}_{1.00}$	$79.00^{11.00}_{11.05}$	$0.50^{0.12}_{0.16}$	$0.36^{0.06}_{0.02}$	197^{121}_{195}	415^{314}_{290}	$1.7^{1.7}_{1.6}$	0.37	1.32

Note. Column: (1) 10^{21} cm^{-2}. Column (2): 10^6 K. Column (3): 10^{54} cm^{-3}. Column (4): km s^{-1}. Column (5): 10^{-13} erg cm^{-2} s^{-1}. Column: (6) 10^{31} erg s^{-1}. N_H = column density; T = X-ray temperature; EM = emission measure; v = line width from individual fits to Ne and Si; f_x = X-ray flux; L_x = X-ray luminosity at 396.5 pc; C_ν = Cash statistic of two APED broadband fit.

4.4.3. Coronal Temperatures

Table 4 shows all the APED temperatures of the spectral fits. Most spectra required two APED components with moderate absorption. About half a dozen sources are so absorbed that we only detect one hot component. The sources with low or moderate temperatures produced a moderately hot APED component of 6–19 MK. The temperatures of APED components are determined by the observed relative line strengths within an ion species and the strength of the underlying continuum. The uncertainties of this temperature component are relatively small, indicating it is well determined specifically due a high number of contributing lines. In that respect the spread in temperature between the ONC stars is likely real.

Figure 10 plots all temperatures against surface flux, and Figure 11 plots the emission measure against all temperatures. The very hot component not only shows quite a large scatter between 30 and 90 MK, but likely a bifurcation of values. It shows the presence of two temperature regimes, one between 30 and 50 MK, and a very hot one between 60 and 90 MK. While in the case of the hot components, there are a few supporting lines from Si, S, Ar, and Ca, the very hot component, at best, has line contributions from Fe XXV and Fe XXVI but is mostly defined by the continuum. Of the highly absorbed stars, there is only one, COUP 662, that exhibited an extremely high-temperature component at 89 MK. At such high temperatures, no lines will be detected as the plasma is completely ionized. Another interesting case is V495 Ori, which is bright in only two observations and exhibits a giant flare. It shows a moderate and a very hot component of 69 MK, indicating that sources with very hot components likely engage in heavy flaring.

It is also important to consider the underlying emission measure contributions. For the two components we measure values between a few times 10^{53} and 10^{54} cm^{-3}. This shows that the ensemble of coronal stars exhibits fairly consistent properties. These are, except for MT Ori, slightly smaller than the ones determined in the early observations (Schulz et al. 2015), but not by much. However, there are some significant trends with respect to X-ray temperature. The first is that on average the emission measures of the low-temperature component (∼10 MK) is about a factor of 2–3 smaller than that of

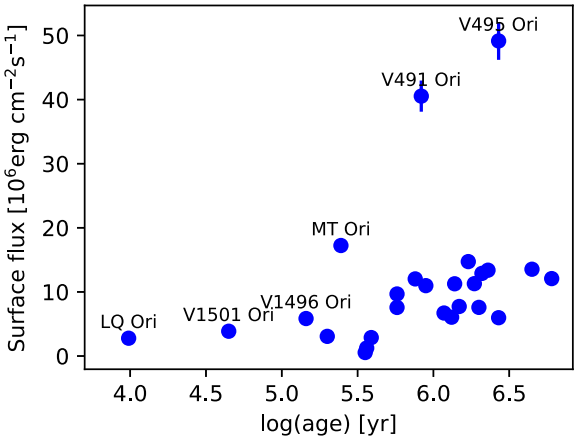

Figure 8. The surface flux plotted against the modeled age of the ONC stars The ages are taken from the COUP tables, the surface flux is the source luminosity divided by the stellar surface area. The latter was determined from the bolometric luminosity and the effective surface temperature, both also from the COUP tables. An interactive version of this figure is available with the ability to zoom, pan, and display the name and additional information for each source. The data necessary to recreate this figure is available in machine-readable format. The data file contains many additional columns, which allows readers to also recreate Figures 9–12. An interactive version of this figure is available.

(The data used to create this figure are available.)

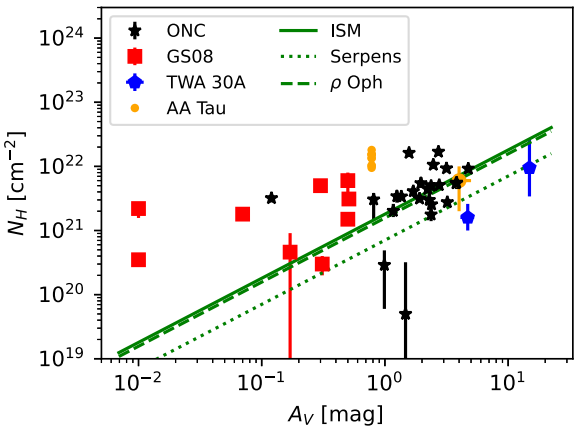

Figure 9. The $N_{\rm H}$ from the APED fits plotted vs. the $N_{\rm H}$ determined from optical extinction A_V in comparison to AA Tau (the small dots without error bars denote measurements before the dimming) and TWA 30A. The red squares are from the sample from Günther & Schmitt (2008, GS08). Green lines show the $N_{\rm H}/A_V$ ratio observed in the ISM and the average value for two other star-forming regions. Data sources are given in Section 4.4.2. Only for AA Tau and TWA 30A extinction and absorption data are contemporaneous, while all other cases rely on optical and X-ray data taken non-contemporaneously. An interactive version of this figure is available with the ability to zoom, pan, and display the name and additional information for each source. Clicking on the legend entries mutes/unmutes the data for better visibility. The data necessary to recreate this figure is available in machine-readable format. The data file contains many additional columns which allows readers to also recreate Figures 8 and 10–12. An interactive version of this figure is available.

(The data used to create this figure are available.)

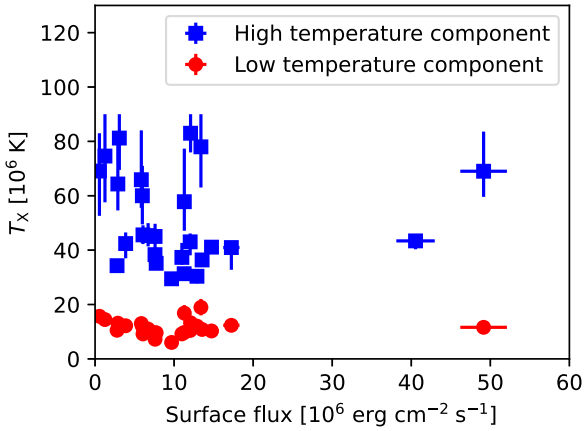

Figure 10. The coronal temperatures from the APED fits vs. the surface flux. An interactive version of this figure is available with the ability to zoom, pan, and display the name and additional information for each source. The data necessary to recreate this figure is available in machine-readable format. The data file contains many additional columns, which allow readers to recreate Figures 8, 9, 11, and 12. An interactive version of this figure is available.

(The data used to create this figure are available.)

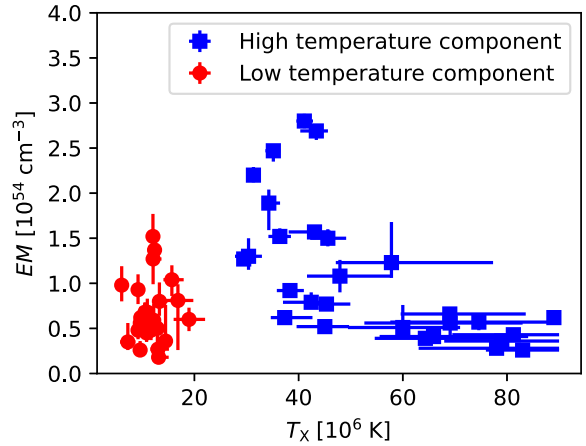

Figure 11. The emission measures from the APED fits plotted vs. the temperatures from the fits. This figure is zoomed in to avoid large values in MT Ori and V450 Ori. An interactive version of this figure is available with the ability to zoom, pan, and display the name and additional information for each source. The data necessary to recreate this figure is available in machine-readable format. The data file contains many additional columns which allows readers to also recreate Figures 8–10 and 12. An interactive version of this figure is available.

(The data used to create this figure are available.)

the hot component (∼40 MK). This is not the case for the very hot component (> 60 MK), which is similar or even lower in value than the one associated with the low-temperature component. Thus it appears that all three X-ray temperature regimes possess distinct properties with respect to their coronal nature with respect to emission volume and maybe even plasma densities.

One item we did not pursue in this global coronal analysis is a more detailed study of abundances, which should be done in more detailed follow-up studies of this coronal sample. However, we did perform a fit of APED abundance values, which can be useful already. However, when we determine a set of average values, we need to optimize the sample. For example, for highly absorbed sources values for Ne and Mg are more unreliable because only a few weak lines might exist. Similarly we might exclude high Z element abundances from the subset of very high-temperature components because lines are weak and/or likely only some Fe K lines exist. In

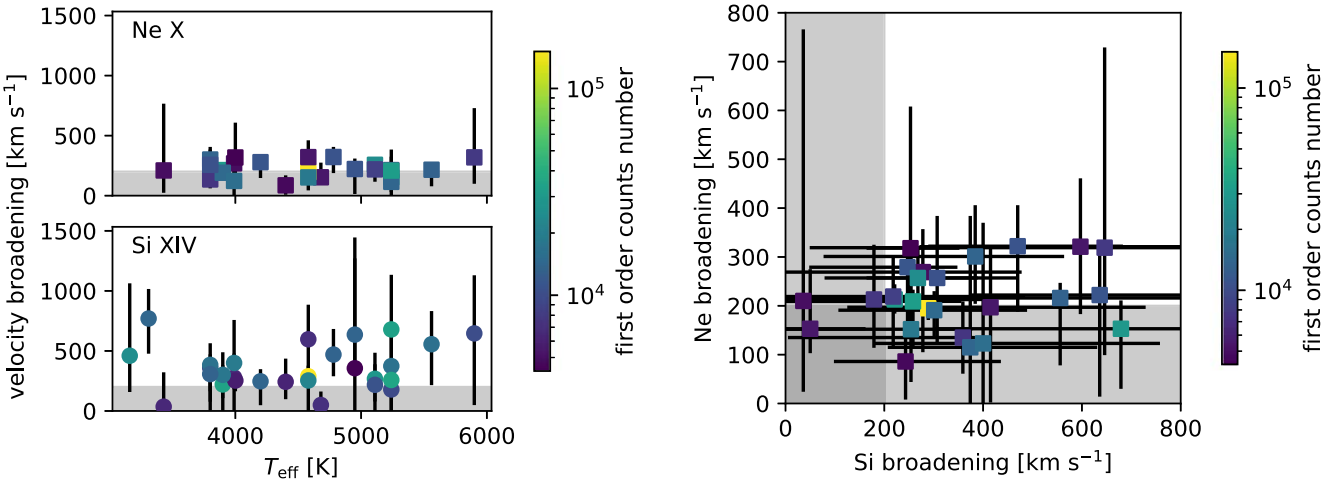

Figure 12. The measured line widths from the single line fits. Gray boxes show the regions where the measured line width cannot be distinguished from instrumental broadening alone. Left: velocity broadening vs. effective temperature. The symbol color indicates how far off-axis the source is located, averaged over all observations. Right: comparison of the velocity broadening in Ne and Si directly. The symbol color indicates the number of counts in the zeroth order for each source. An interactive version of this figure is available with the ability to zoom, pan, and display the name and additional information for each source. Clicking on the legend entries mutes/unmutes the data for better visibility. The data necessary to recreate this figure is available in machine-readable format. The data file contains many additional columns which allows readers to also recreate Figures 8–11. An interactive version of this figure is available.
(The data used to create this figure are available.)

calculating the average values for the remaining sources, we also drop the highest and lowest values to remove some bias where the fit was unable to make a sensible determination. The average abundance distribution for the coronal fits then yields the following values with respect to solar (Anders & Grevesse 1989): Ne (1.52 ± 0.70), Mg (0.18 ± 0.16), Si (0.20 ± 0.13), S (0.28 ± 0.21), Ar (0.59 ± 0.45), Ca (0.26 ± 0.25), and Fe (0.14 ± 0.18). The $\pm$ values are not uncertainties but the variance from the average in the sample. These abundance ranges are consistent with the abundances stated in Schulz et al. (2015; see also Maggio et al. 2007 for the COUP results).

4.4.4. Line Broadening

We also performed separate line fits to the bright lines in the spectrum. The best cases were the Ne X and the Si XIV lines, both H-like single line systems. We ignored the spin–orbit coupling and fitted these lines with single Gaussian line functions at the appropriate wavelength. Here, we also have to worry about the spatial distribution of sources. The stars in Table 2 distribute around the aimpoint within about 3′ radius. The HETG instrument can tolerate zeroth orders to about 2′ off-axis and not suffer degradation of spectral resolution. This means that about 25% of the stars in Table 2 will suffer some form of spectral degradation. We plotted all line fits and color coded the off-axis information (left panel of Figure 12) and number of counts in the first order (right panel). Stronger sources are generally measured better, but the flux in the relevant lines also depends on the spectral shape. The figure shows a general trend where sources with broadened Ne lines also have broadened Si lines, though the error bars are also compatible with no measurable broadening for most sources.

To further quantify line broadening, since we do not expect it in typical coronal sources, we took one case to investigate in more detail. MT Ori has well-detected broadening in Ne X. We started with the two-temperature plasma model (see Table 4) and allowed the turbulent broadening term and the redshift to

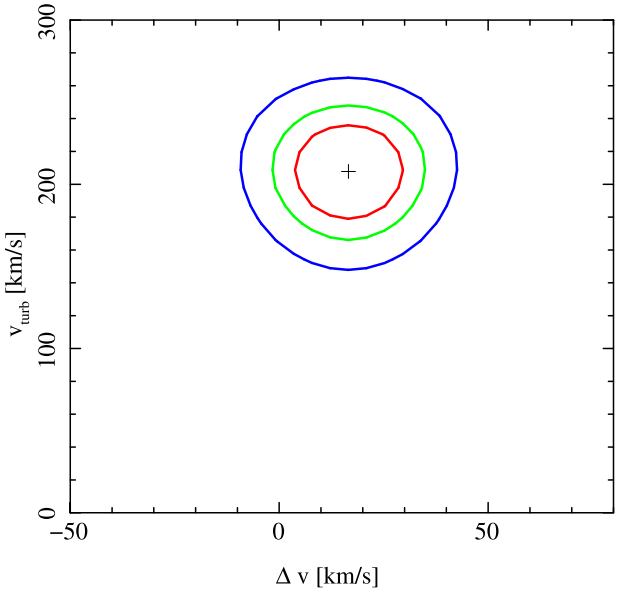

Figure 13. The confidence contours for the turbulent broadening term against Doppler shift for a plasma model fit to the 8–14 Å region of MT Ori. Contours are for the 68%, 90%, and 99% limits.

be free parameters and refit the merged spectrum over the 8–14 Å region where there are many lines from Mg, Ne, and Fe. We also let the normalization float (but tied the ratio), but kept the two temperatures frozen. In addition, we allowed relative abundances of Mg, Ne, and Fe to be free. In this way, we implicitly include all blending implicit in the model, account for thermal broadening, and determine any excess broadening required to fit the spectrum. This confirms the result found for fitting individual features. We show the confidence contours of the excess broadening against the Doppler shift in Figure 13, and the contours are closed. This is a barely resolved result—if the broadening were a bit lower ($v_{\rm turb} \gtrsim 100\,{\rm km\,s^{-1}}$), then the contours would likely be unbounded on the lower

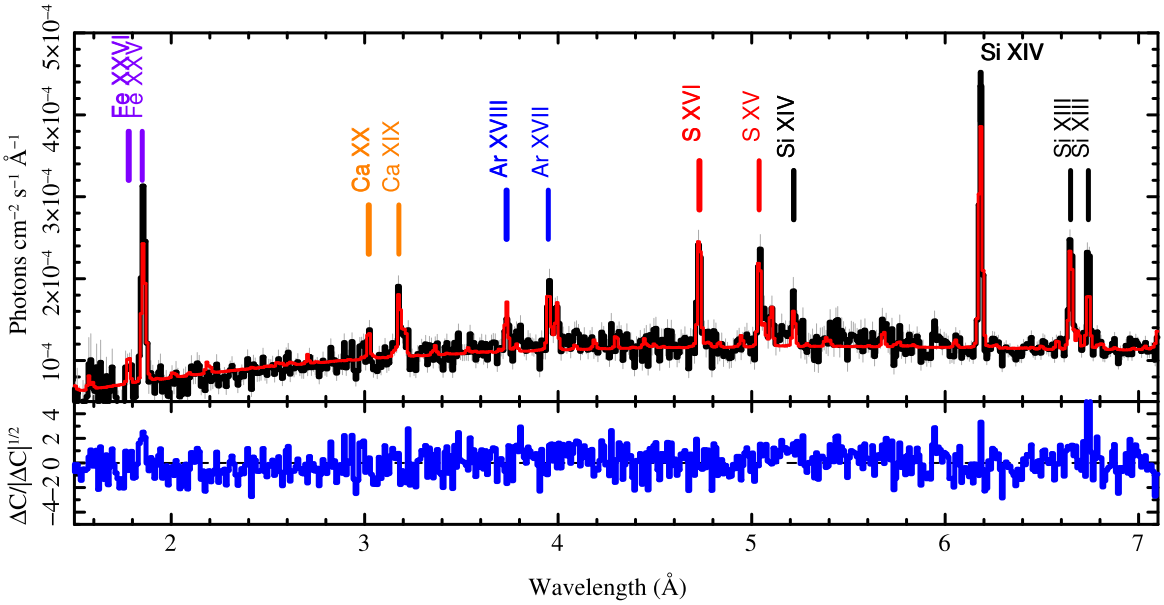

Figure 14. The short-wavelength region HETGS spectrum of θ^1 Ori E, having an effective exposure of 1.5 Ms. The prominent H- and He-like emission lines are labeled. The flux spectrum is shown in black, the model in red, and residuals in the lower panel. Line label colors are arbitrary.

Table 5
Broken Power-law Emission Measure Model Parameters

Parameter	Value
Norm	6.3×10^{-3} (1.0×10^{-4}) [cm^{-5}]
$T_{\max}$	26.3 (2.4) MK
α	0.9 (0.1)
β	−2.5 (0.2)
O	0.22 (0.08)
Ne	0.82 (0.08 :)
Mg	0.30 (0.03 :)
Si	0.22 (0.02 :)
S	0.25 (0.04 :)
Ar	0.58 (0.1 :)
Ca	0.84 (0.2 :)
Fe	0.17 (0.01)
Ni	0.11 (0.06)

Note. Model parameters, for an emission model defined by $\mathrm{EM}(T) = \mathrm{Norm} * (T/T_{\max})^{a(T)}$; $a(T < T_{\max}) = \alpha$; $a(T \geqslant T_{\max}) = \beta$. Elemental abundances are given relative by number to the fiducial values of Anders & Grevesse (1989). The emission measure and normalization are related in the usual scaling: $\mathrm{EM} = 10^{14} \times \mathrm{Norm}/(4\pi d^2)[\mathrm{cm}^{-3}]$. Abundance uncertainties not formally evaluated but estimated from counts are designated with a ":".

limit. We suspect that broadening in this case could be due to orbital motions in a binary system.

4.4.5. θ^1 Ori E

θ^1 Ori E is a spectroscopic binary with a 9.9 day period in which both components, each a G-type giant, have an intermediate mass of about 2.8 $M_\odot$ (Morales-Calderón et al. 2012). The basic characteristics were reviewed by Huenemoerder et al. (2009), along with a detailed analysis of the HETG spectrum. We now have an effective exposure of about 1.5 Ms, compared to the previous 260 ks. Due to detector efficiency reduction and source confusion, the largest exposure gains are in the short-wavelength region, below 10 Å, and we fully realize the expected increase in S/N of 2 or more. This will allow us to put better constraints on the highest temperature plasma through the continuum emission and the emission from the H- and He-like ions of Si, S, Ar, Ca, and Fe. Here, we provide an overview of the improved spectrum, with a look at an approximate plasma model, variability, and line profiles.

A three-temperature APED model provided an overall characterization of this high brilliance spectrum, but as we noticed for θ^1 Ori C, there were large residuals that could not be eliminated with few-temperature-component models. We thus adopted a broken power-law emission measure distribution model, which approximates the line-based emission measure reconstruction of Huenemoerder et al. (2009). The model parameters are the normalization, the temperature of the maximum emission measure, and power-law slopes below and above that temperature, and relative elemental abundances; fitted values are given in Table 5. Uncertainties for the emission measure shape were determined from a Monte Carlo evaluation, with relative abundances frozen. The Fe and Ni values were determined post facto from confidence levels determined using only the 10–13 Å region, which has many Fe lines and the brightest Ni lines. The oxygen abundance uncertainty was scaled from the flux uncertainty, and is the most uncertain value due to the low counts in that region, due both to line-of-sight absorption and detector contamination. Portions of the spectra and models are shown in Figures 14 and 15.

The plasma model fits include a *turbulent* velocity term and a redshift. Emission lines were also fit individually with Gaussian profiles. The lines in the merged spectrum showed significant excess broadening (in addition to instrumental or thermal terms), having about 400 km s^{-1} full width-half-maximum with an uncertainty of 50 km s^{-1} (corresponding to $v_{\mathrm{turb}} \approx 200 \pm 30$ km s^{-1}). The maximum orbital radial velocity separation is about 160 km s^{-1}. Since the spectrum fit was merged over all observations, we expect there to be some width due to orbital dynamics. However, the measured width is somewhat larger than expected from photospheric radial velocities alone. The mean profile Doppler shifts are consistent

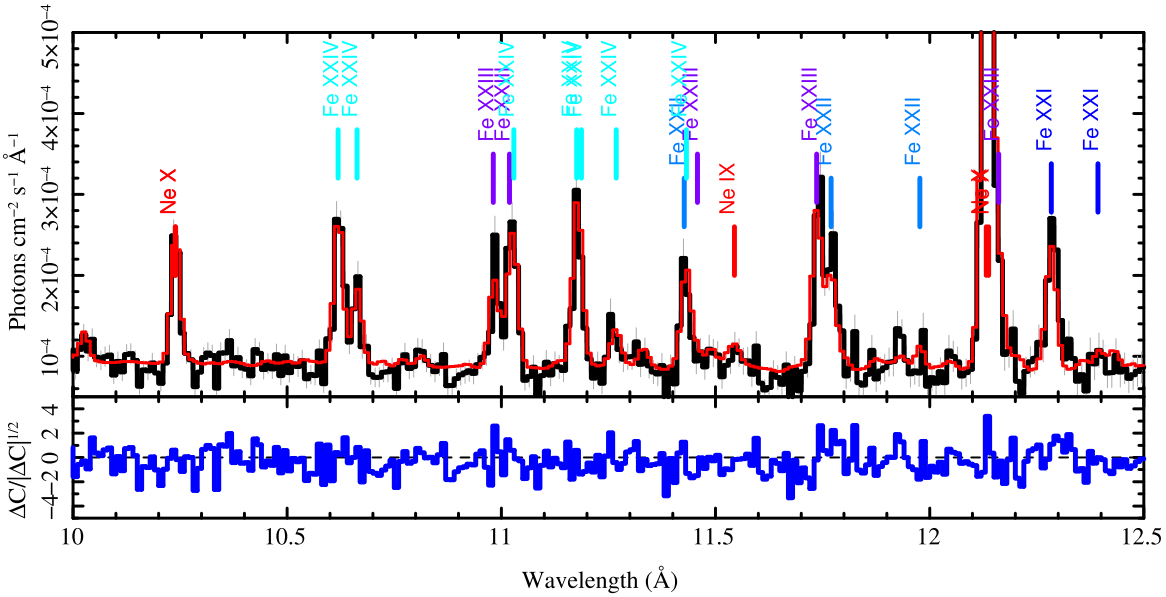

Figure 15. The 10–13 Å region HETGS spectrum of θ^1 Ori E, which is important for establishing the relative Fe and Ni abundances, given the emission measure model. The fluxed spectrum is shown in black, the model in red, and below are the residuals. Prominent emission from Fe XXI to Fe XXIV are labeled, as well as some neon lines (label colors are arbitrary).

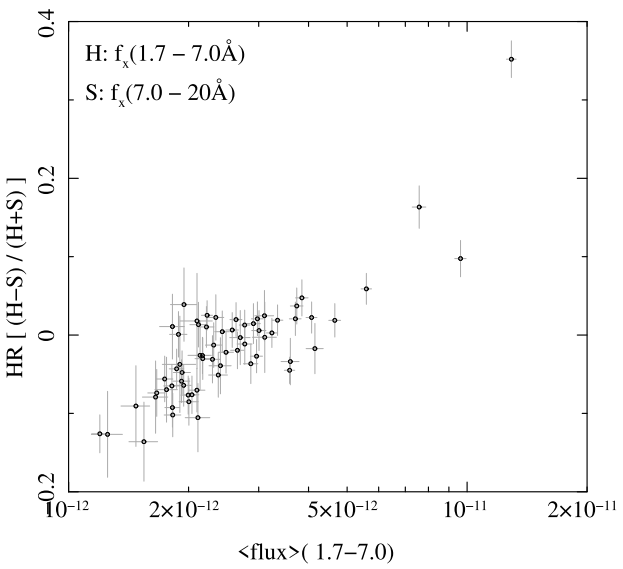

Figure 16. The HR vs. hard flux for θ^1 Ori E. Each point represents a single observation ID. A hardness increasing directly with flux is a characteristic of stellar coronal flares (magnetic reconnection events). Flux is in units of erg cm^{-2} s^{-1}.

with 0.0 ± 30 km s^{-1} (not accounting for heliocentric motion). The values are consistent with Huenemoerder et al. (2009), but have smaller uncertainties. The widths and offsets definitely need further scrutiny, especially relative to the orbital phase.

With this deeper exposure of θ^1 Ori E, we have significantly improved diagnostics from the 2–7 Å region, specifically from the emission lines of Si, S, Ar, and Ca. The broken power-law emission measure model, though, may be too simple since the model seems to underpredict Fe XXV, as can be seen in the residuals in Figure 14.

θ^1 Ori E is highly variable**.** As a broad overview of this, we fit the mean flux in a hard band (1.7–7.0 Å) and in a soft band (7.0–20.0 Å) and formed a hardness ratio, HR $= (H - S)/(H + S)$, where H and S refer the hard and soft band fluxes. In Figure 16, we plot the HR against H for each individual Chandra observation. This shows over an order of magnitude range in H, in a direct correlation with HR. The flux-hardness trend is likely due to coronal magnetic flare events. This is consistent with one of the defining characteristics of stellar coronal (magnetic) flares, that they are hotter and brighter.

The abundance of Ne seems significantly larger than determined by Huenemoerder et al. (2009), either due to flaring, or could be due to emission measure distribution structure, which will require more careful evaluation using reconstruction using line fluxes, or via exploration of more complex emission measure models. Abundances of Ca, Ar, and Ni are consistent with the upper limits of previously determined values but are now much better constrained.

5. Summary and Outlook

This data set was designed to provide the first collection of high-resolution X-ray spectra of a very young massive stellar cluster. We were able to harvest about three dozen high-resolution X-ray spectra from young massive, intermediate-mass, and low-mass stars with sufficient statistical properties to determine spectral fluxes, coronal temperatures, line widths, line ratios, and abundances. This data set now provides a unique base of high-resolution X-ray spectra of some of the youngest stars known. The ONC cluster study provides common initial conditions for all extracted objects: stars are chemically similar, they have young ages, a common ISM evolution, and are exposed to fairly similar global extinction. This first extraction is designed to provide average properties of extracted stars, it does not yet allow to extract time slices needed for flare studies, for example.

The sample of extracted HETG spectra includes four massive stars. The most prominent star is θ^1 Ori C (Schulz et al. 2000, 2003; Gagné et al. 2005) with over 10^6 of total counts in first order, providing for the high S/N at the provided oversampling of each HETG resolution element, which will

allow for high brilliance line profile studies and weak line searches (see M. Gagné et al. 2024, in preparation). One of the most intriguing outcomes of the long exposure for this star is the potential use of higher order grating data, which in this case resolves high Z He-like triplets of Mg, Si, S, Ar Ca, and Fe with unprecedented high resolution. Plasma density and UV pumping studies should be highly beneficial for future high-resolution missions. θ^2 Ori C is the second most massive star in the sample, and here, the survey added only about 10^4 cts to the previously existing data as published in Schulz et al. (2006) and Mitschang et al. (2011). The new data should primarily improve the study of Mg and Si lines. The zero-order data shows high variability in the source, indicating that the star system did engage in flaring activity as reported in Schulz et al. (2006), and while the HETG first order covers only a fraction of this activity, it should prove essential in the in-depth flare analysis. Another interesting but also unfortunate outcome of the survey is the almost complete absence of θ^1 Ori D in HETG first order and also a surprising weakness in the zeroth order. The latter is likely a result of the fact that softer X-rays are blocked by detector contamination. More interesting is the collection of over 7×10^4 cts in θ^1 Ori A, a massive trapezium star that is with respect to primary spectral type as well as the number of companions very similar to θ^1 Ori D, a fact that certainly needs further study. The fifth massive star in the sample is V1230 Ori, which is not part of the Orion Trapezium and is farther away in the ONC. Since the survey could not produce any first-order spectra for θ^1 Ori B and θ^2 Ori B, the 2.4×10^4 cts in HETG first order are the only data to study later B-type massive stars.

The survey also produced over 30 HETG first-order spectra of intermediate-mass and low-mass CTTS, which at their current evolutionary state, should exhibit accretion and coronal signatures. At a canonical age of the ONC of around 1 Myr and older, we expect mostly the latter. The θ^1 Ori E binary and MV Ori are the most massive among the stars in this sample. The deeper exposure of θ^1 Ori E improves the determination of the high-temperature emission measure and elemental abundances through the well-detected emission lines of Si, S, Ar, Ca, and Fe in the 1.8–7 Å spectral region. The longer exposure also better quantifies the variability as typical of coronal flares. Future work is needed to improve the emission measure distribution, since it probably has more structure than the model adopted here, to study the distribution at different emission levels to help model flaring structures, and to phase resolve line-shifts and broadening to further model the emission from each stellar binary component.

We analyzed all the non-massive stars with a two-temperature coronal plasma model to characterize their global coronal properties. From these fits, we determined X-ray fluxes between 1.3×10^{-13} and 3.4×10^{-12} erg cm^{-2} with the bulk of the fluxes trending more to the low end of these limits. Most ONC stars are even fainter. It is important to note that more exposure would not result in additional sources with successfully extracted first-order spectra as source confusion becomes more dominant. Table 2 shows that some extraction efficiencies are already well below 0.5 and final exposures well below 50%, indicating that spectral extraction becomes very inefficient. In that respect this survey is going to the limit of what the high-resolution gratings can achieve in a crowded cluster field.

From the extracted sample we can see that if we describe X-ray activity in terms of surface flux, then Figure 8 might show that activity increases with age in CTTS, even though not as strongly as was suggested in Schulz et al. (2015). The surface fluxes of the bulk of the ONC stars appear quite similar to other CTTS stars. What is striking in these global fits is the distribution of coronal temperatures. A large number of ONC stars can be described by a bimodal temperature distribution, where one temperature is around 10 MK, and the other one more around 40 MK. This is what Schulz et al. (2015) observed in the six bright ONC CTTS and is no surprise. It is observed in many other CTTS outside the ONC, such as TW Hya (Kastner et al. 2002), HD 9880 (Kastner et al. 2004), and BP Tau (Robrade & Schmitt 2006), to mention a few of the many we know today. Here, we see these common properties in almost three dozen T Tauri stars of a single cluster. What is new is that there is a subsample of sources where the high-temperature component is more like 60 MK and higher, something that is not expected under normal coronal conditions. This definitely requires further study. It is interesting to note that the emission measures of the two normal temperature components distribute somewhat similarly to what was projected in Schulz et al. (2015) but not as extreme; the average between high and low temperatures differs more like 2.5 instead of the factor of 3–6. However, it should be noted that in the cases of the very high temperatures, the emission measures are systematically low, indicating that here, we may deal with high plasma densities and low volumes. We should add that very high temperatures have been reported with ASCA (Tsuboi et al. 1998) and the COUP project (Getman et al. 2005; Maggio et al. 2007). Here, we confirm the high temperatures with a high-resolution dispersive device.

CTTS are also characterized by active accretion, and in some nearby stars with low absorption, accretion signatures are seen prominently in the grating spectra: the line ratios in the He-like triplets of O VII and Ne IX have unusually low forbidden to intercombination (f/i) line ratios, that can only be explained by high densities in the emission region (Kastner et al. 2002; Brickhouse et al. 2010). The observed densities are higher than seen in the corona and do not correlate with flares, thus a natural explanation is for the emission to come from the cooling flow behind the accretion shock. Unfortunately, the data presented here cannot be used to test for this, as the high contamination on the ACIS camera makes those lines inaccessible to us. The other signature of accretion seems to be an excess of soft plasma when comparing accreting and non-accreting CTTS (Robrade & Schmitt 2007; Telleschi et al. 2007), which could again be a direct signature of the post-shock cooling flow or an indirect effect where the presence of accretion columns cools or distorts the fields in the corona (Schneider et al. 2018). Again, the low sensitivity of ACIS in our observations and the high absorbing column densities for many objects in the ONC make it hard to test for this conclusively.

The X-ray absorbing column density and the optical/IR extinction (or *reddening*) probe different aspects of the material in the line of sight. The optical extinction is typically expressed as dimming in a certain band, e.g., A_V, and it is caused by small dust grains. The X-ray absorption is dominated by inner-shell absorption of heavy elements with contribution from H and He; this absorption occurs both in gas and small dust grains. Only large grains that block all energies of X-ray light do not change the shape of the observed X-ray spectrum; instead, they cause gray absorption that just reduces the overall intensity. The

X-ray absorbing column density is measured as N_H, the equivalent hydrogen column density that would cause the observed absorption for some standard set of elemental abundances. A naive interpretation of the N_H/A_V ratio is that this measures the gas-to-dust ratio averaged over the line of sight. However, grain growth and non-standard abundances also influence the measured ratio and might be different in the accretion columns, the disk atmosphere, the cloud material, and the ISM between the ONC and Earth.

One promising approach is to study time variability, where the timescale can give us a hint as to which region the absorber is located. Principe et al. (2016) observed a change in N_H over a month, but with a constant N_H/A_V ratio in TWA 30. This star is seen nearly edge-on, so we are looking through some layers of the disk, with different column densities at different times or locations, but constant dust grain properties. In AA Tau, Grosso et al. (2007) observed repeated changes of N_H over the 8 day rotation period consistent with a wedge of the inner disk rotating in and out of view; this inner part of the disk appears gas-rich, while an outer ($R > 1$ au) dimming indicates ISM-like material (Schneider et al. 2015). Another prominent example is RW Aur (Günther et al. 2018), which showed an increase in N_H by a factor >100 over timescales of months to years, clearly related to major changes in the disk structure. In our general analysis in the ONC, we do not have the time information as in these examples, but we can look at the properties of the sample. Figure 9 shows ONC sources both above and below the line of an ISM-like N_H/A_V ratio. While there are certain systematics in the measurement of both N_H and A_V, this spread is likely real and represents the different viewing geometries. If the line of sight passes through a structure close to the star, within the dust sublimation radius, N_H/A_V is large. For a star seen at a high inclination angle, the structure could be a polar accretion column, while for stars at a lower inclination, the inner disk might contribute. On the other hand, stars seen through the outer disk might have more evolved dust grains, leading to low N_H/A_V values. Since disks are dynamic, this processed dust can be lifted into higher layers of the disk and might be in the line of sight, even if we do not view the star through the disk midplane.

Of the 45 stars in this study, 33 are known variables, seven are suspected variables, four have not been identified as variable, and one was excluded due to pileup in the zeroth order. These statistics will allow us to carry out a time-resolved analysis of a significant number of flares in a population of cool stars of approximately the same age. For several of the identified flares, high-resolution spectra can be obtained starting before the flare begins to be visible in the X-rays and continuing through the end of the X-ray emission of the flare. Such an analysis technique is rare in the study of flares due to their unpredictable nature. The flare spectra will be analyzed to determine spectral changes during the flares.

The percent of ObsIDs that are probably or definitely variable for each source ranges from 0% to 36%. Of course, the longer the exposure time of an ObsID, the greater the possibility of detecting variability. However, the statistics for each source include the same set of ObsIDs (except those with known zeroth-order confusion) of the same exposure time, so the variability percent is relevant and should be considered in concert with the presence of flares and periodicity. Light curves produced by the `glvary` tool for each ObsID are being evaluated to verify the timing and duration of flares detected by the statistical method.

Acknowledgments

This project was funded by Chandra grant GO0-21015A and by NASA through the Smithsonian Astrophysical Observatory (SAO) contract SV3-73016 to MIT for Support of the Chandra X-Ray Center (CXC) and Science Instruments. CXC is operated by SAO for and on behalf of NASA under contract NAS8-03060. N.S. would like to thank MKI postdoctoral associate Jun Yang for their participation and comments. J.N. acknowledges the assistance of Thomas Firnhaber (University of Kansas) in the zeroth-order variability analysis. The research of T.P. was partly supported by the Deutsche Forschungsgemeinschaft (DFG; German Research Foundation) in the research unit *Transition Disks* (Ref No. 325594231—FOR 2634/2—TE 1024/2-1) and in the Excellence Cluster ORIGINS—EXC 2094-390783311. T.P. would like to thank the LMU PhD students S. Flaischlen and C. Göppl for their assistance in the preparation of data tables for this project. The team would also like to thank Wayne Waldron for helpful comments early in the project.

Appendix A
Light Curves

This appendix contains the concatenated, time-ordered zeroth-order light curves for each source in Table 2. The plots are shown in Figures A1–A4. The data have been binned at 1 ks and time gaps between observations have been eliminated. Time on the x-axis is the cumulative observing time since the beginning of the first observation. Data for ObsIDs where confusion affects the zeroth-order count rate have been eliminated in the plots. Therefore, each point on each plot is derived from a non-confused zeroth order. The vertical dotted line in each plot indicates the significant time gap of about 12 yr in observations. The name of each source is in blue in the upper right-hand corner of each plot. An example plot for LQ Ori is included in the text (Figure 4) and not repeated in this appendix.

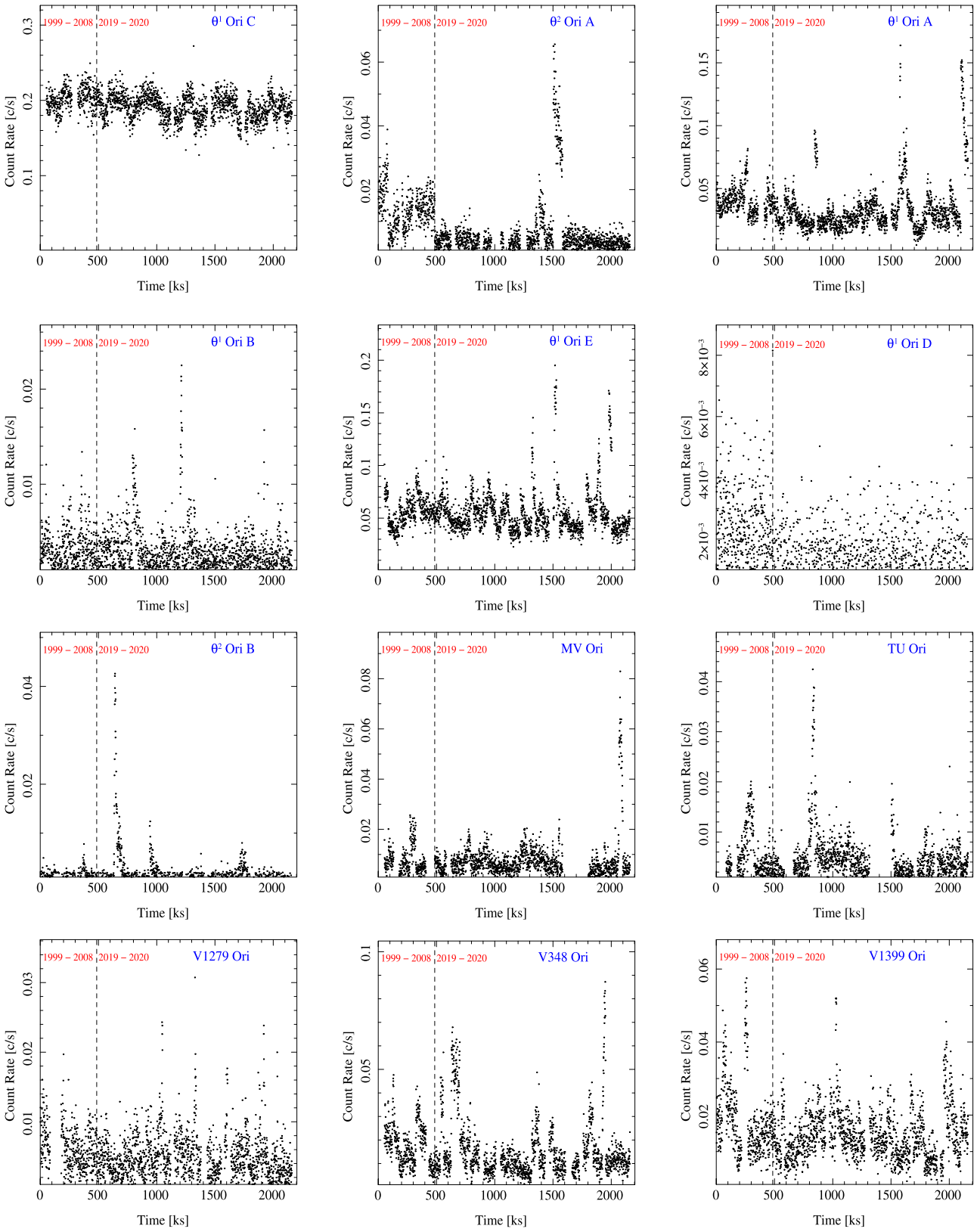

Figure A1. Concatenated light curves as in Figure 4.

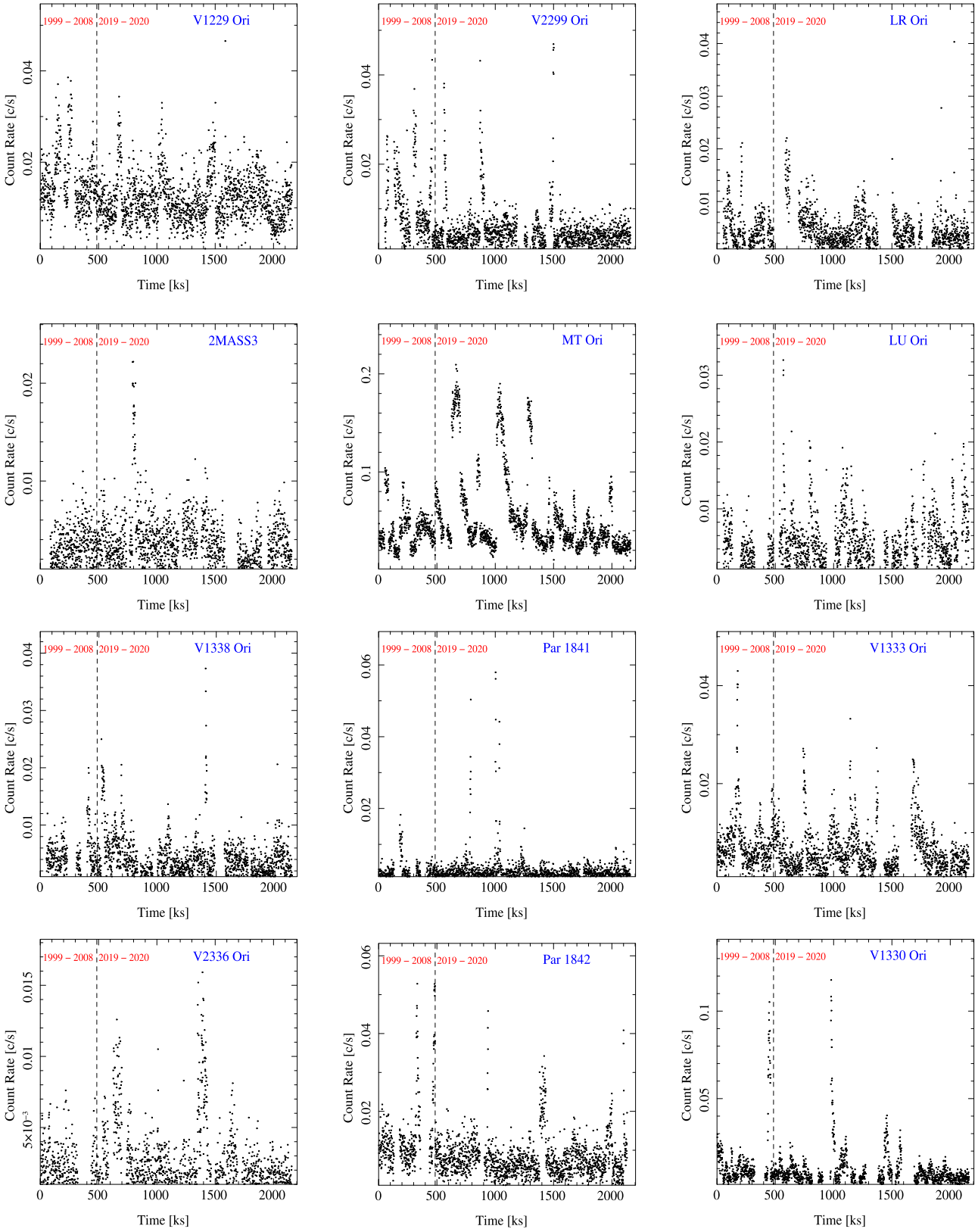

Figure A2. Concatenated light curves as in Figure 4 (continued).

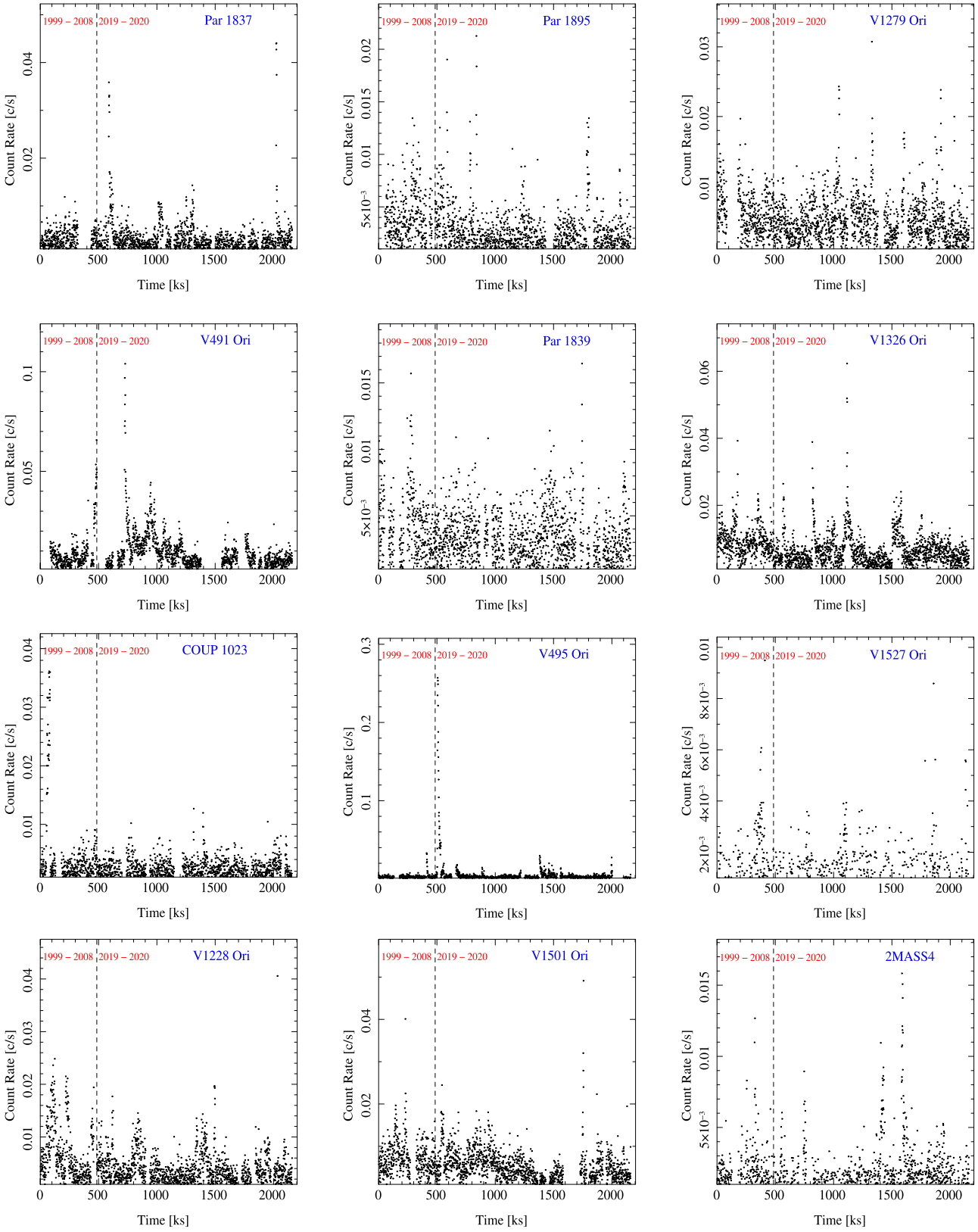

Figure A3. Concatenated light curves as in Figure 4 (continued).

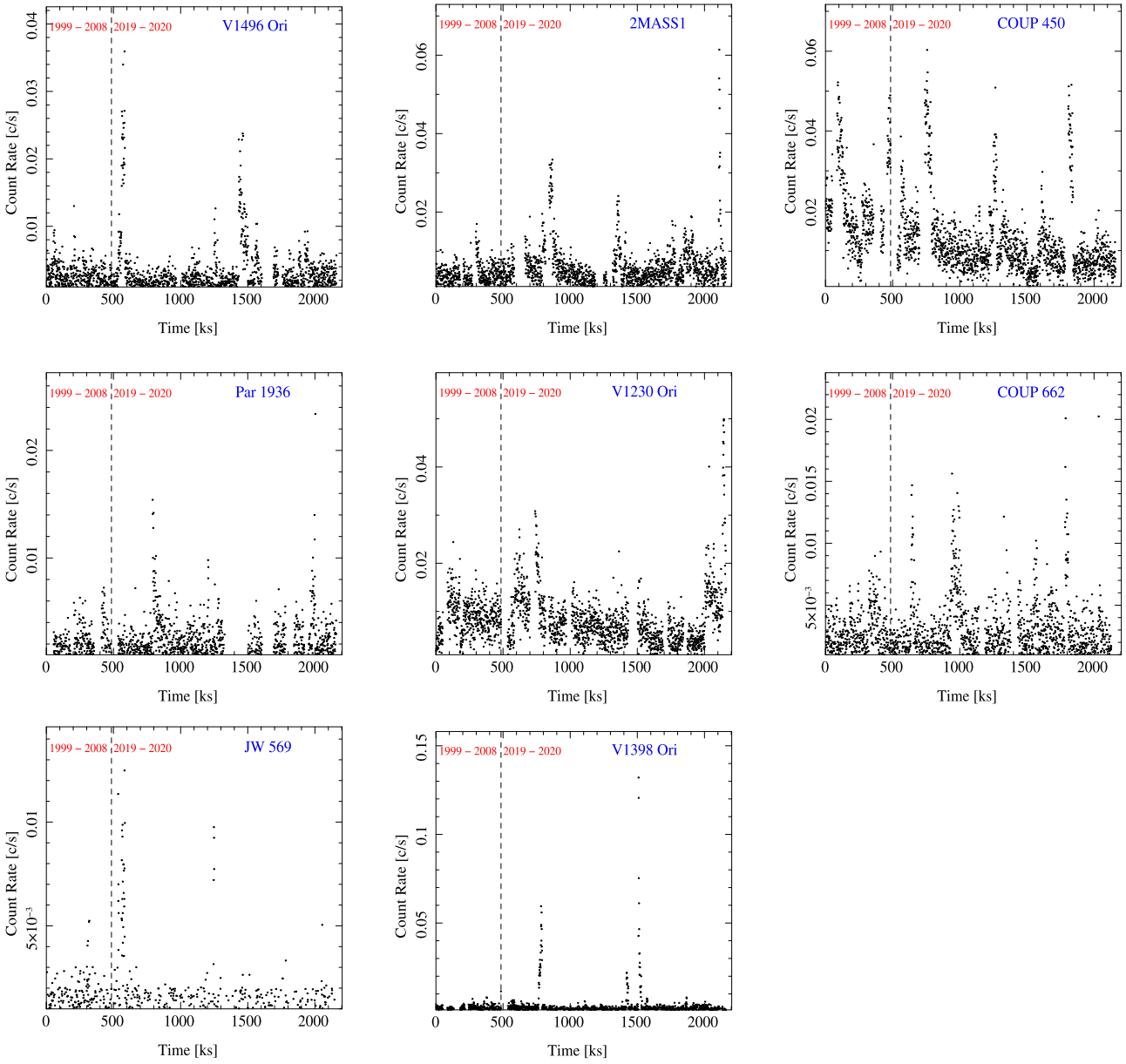

Figure A4. Concatenated light curves as in Figure 4 (continued).

Appendix B
HETG Spectra

In this appendix, we provide plots of all the HETG spectra we extracted so far for this study. The plots are shown in Figures B1–B7. Here, we do not include the HETG spectra we already showed in the main part of the paper, i.e., θ^1 Ori C, θ^1 Ori E, and COUP 450. Merged HEG and MEG spectra are binned to a minimum of 0.01 Å. Some low-signal spectral regions have coarser binning. We note that this was done for plotting purposes only. We also added line identification where it was deemed appropriate. This was done by visual inspection. At first all lines that were identified in the APED database are labeled. However, in some cases, we added identifications in cases where lines that should have been detected were not there. The first three panels are the other massive stars, θ^1 Ori A, θ^2 Ori A, and V1230 Ori. The remaining panels are spectra from extracted intermediate and low-mass stars. The HETG first-order data can be downloaded from the Chandra archive[15] and Zenodo.[16]

[15] https://cxc.harvard.edu/cda/contributedsets.html
[16] doi:10.5281/zenodo.10853416

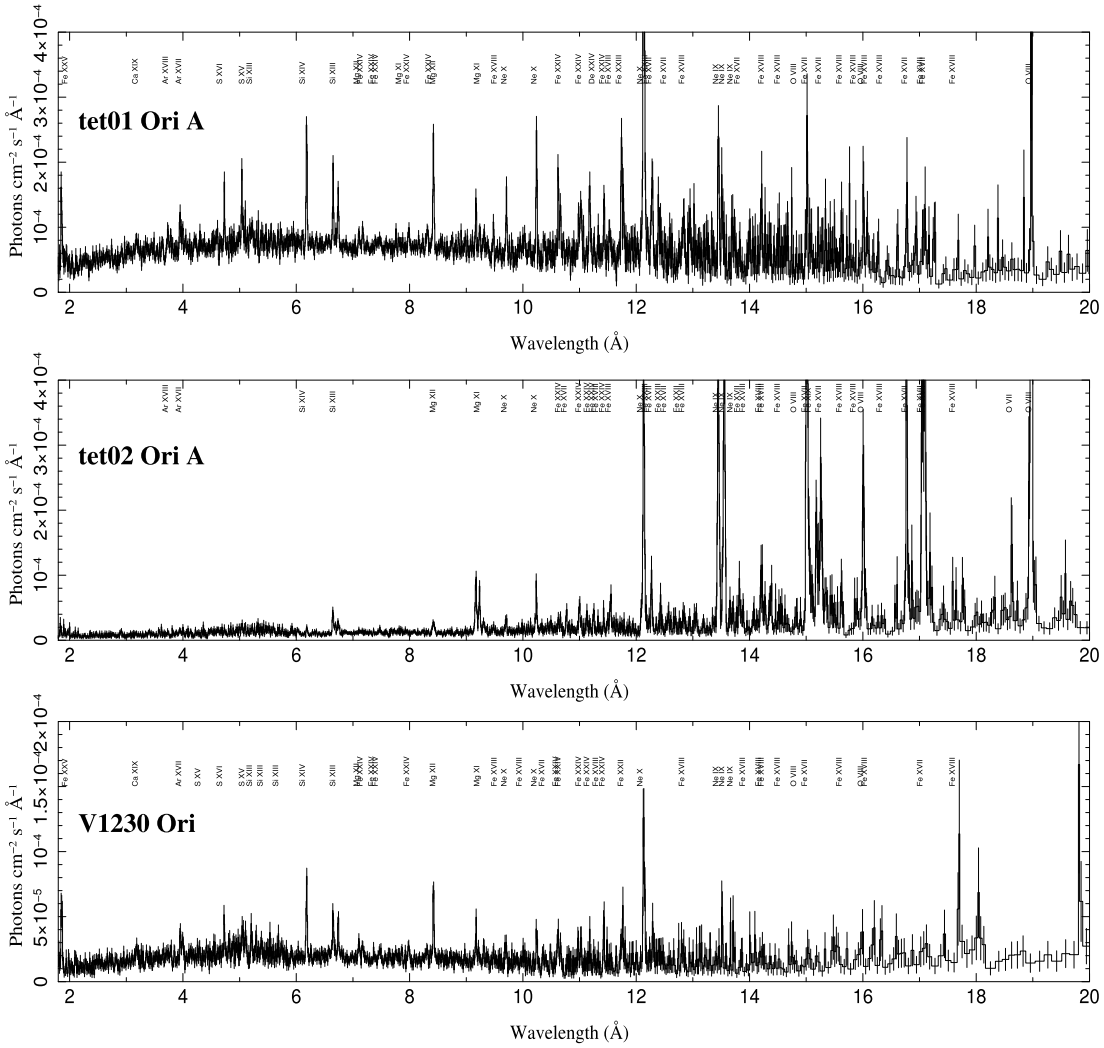

Figure B1. The broadband 2.1 Ms spectra of the other massive stars.

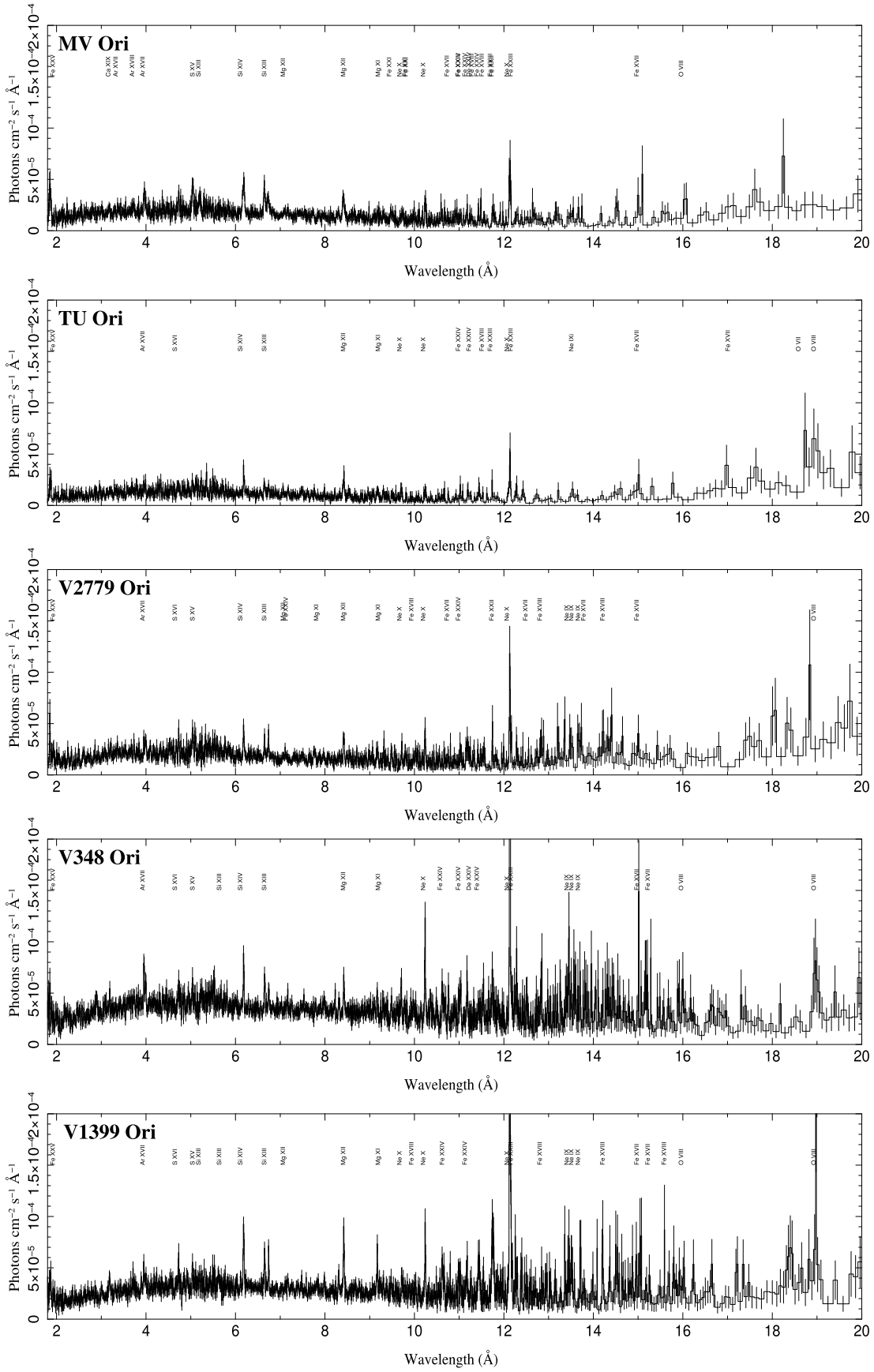

Figure B2. The broadband 2.1 Ms spectra of low- and intermediate-mass stars.

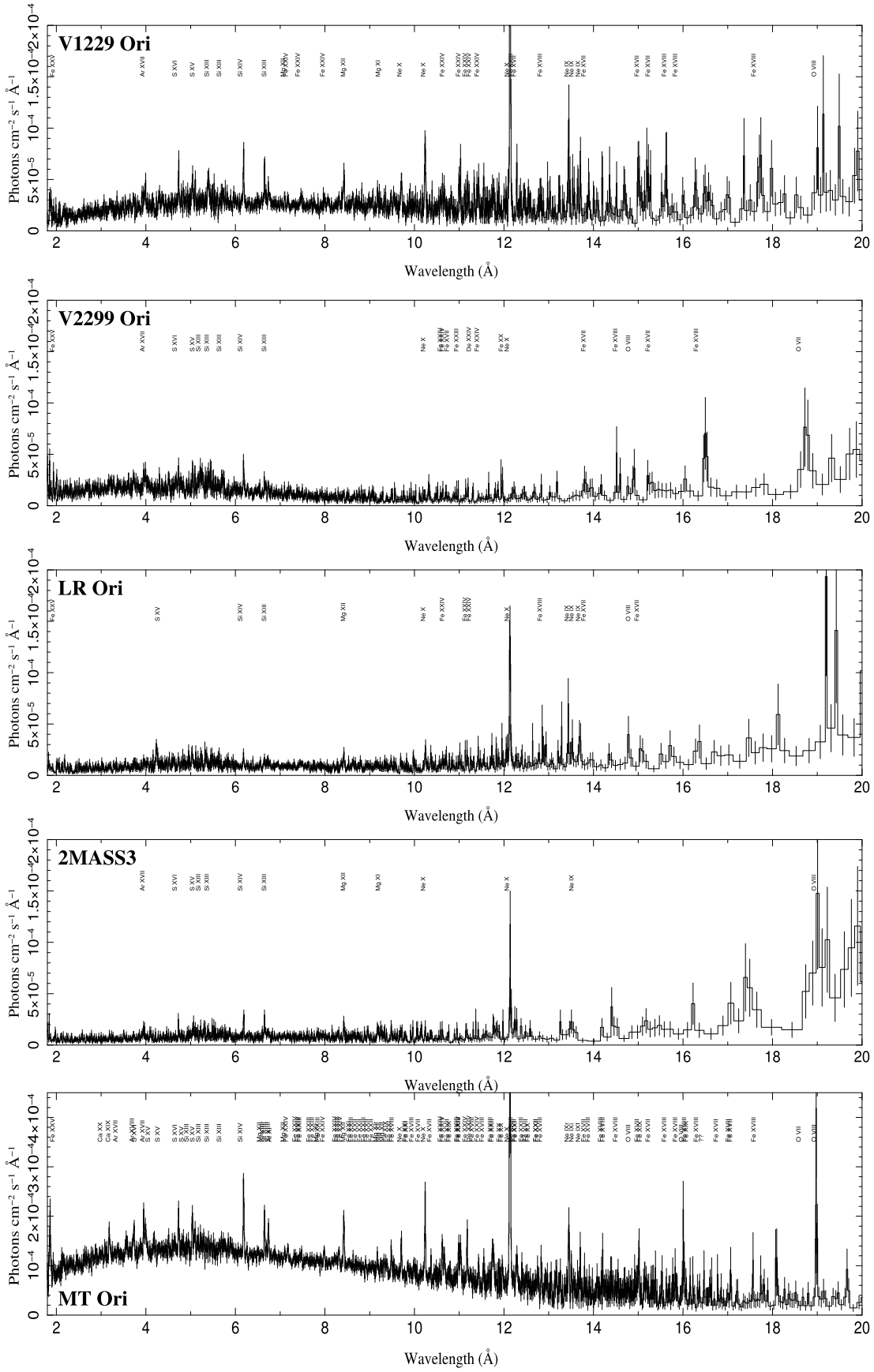

Figure B3. The broadband 2.1 Ms spectra of low- and intermediate-mass stars (continued).

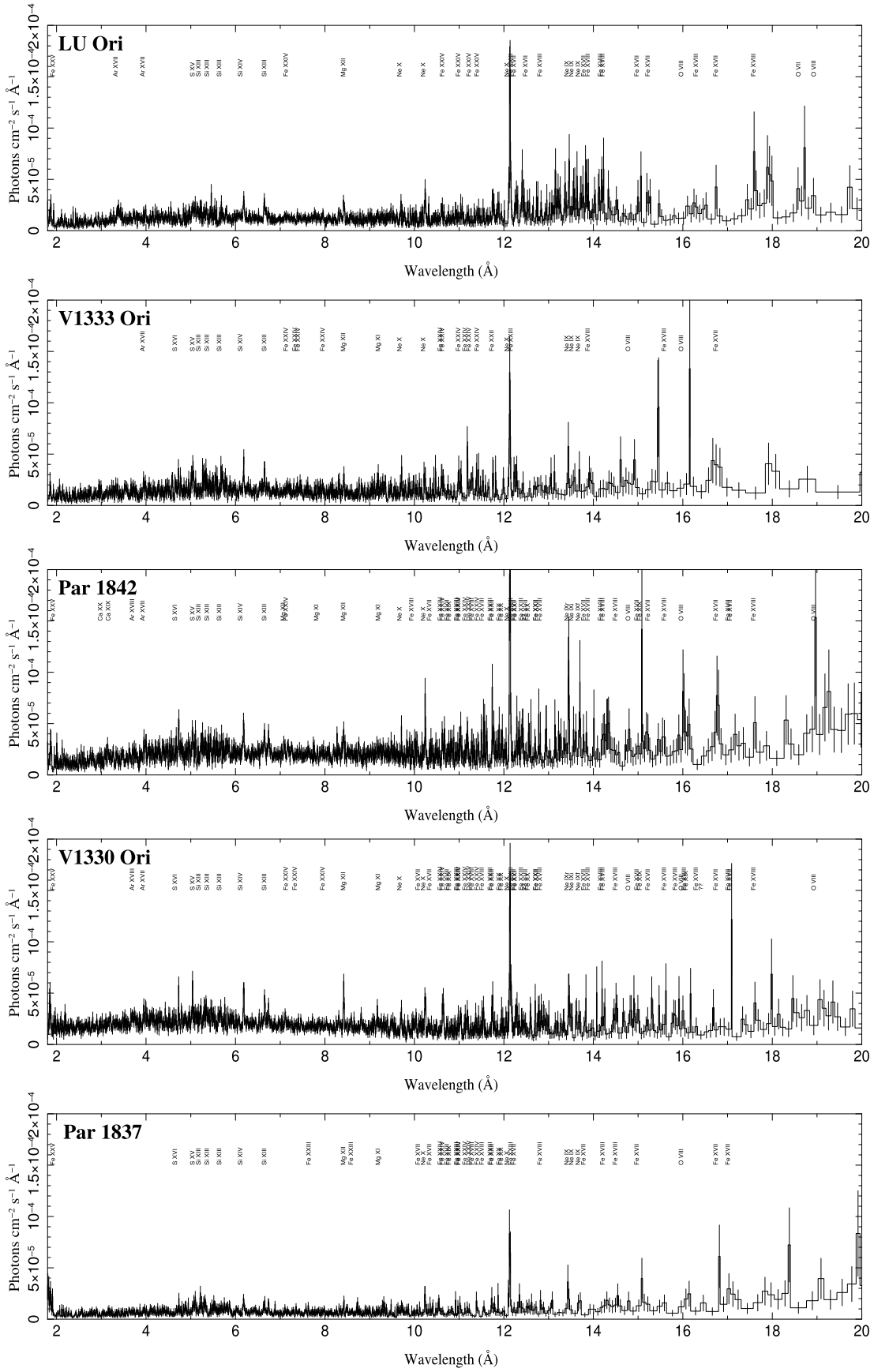

Figure B4. The broadband 2.1 Ms spectra of low- and intermediate-mass stars (continued).

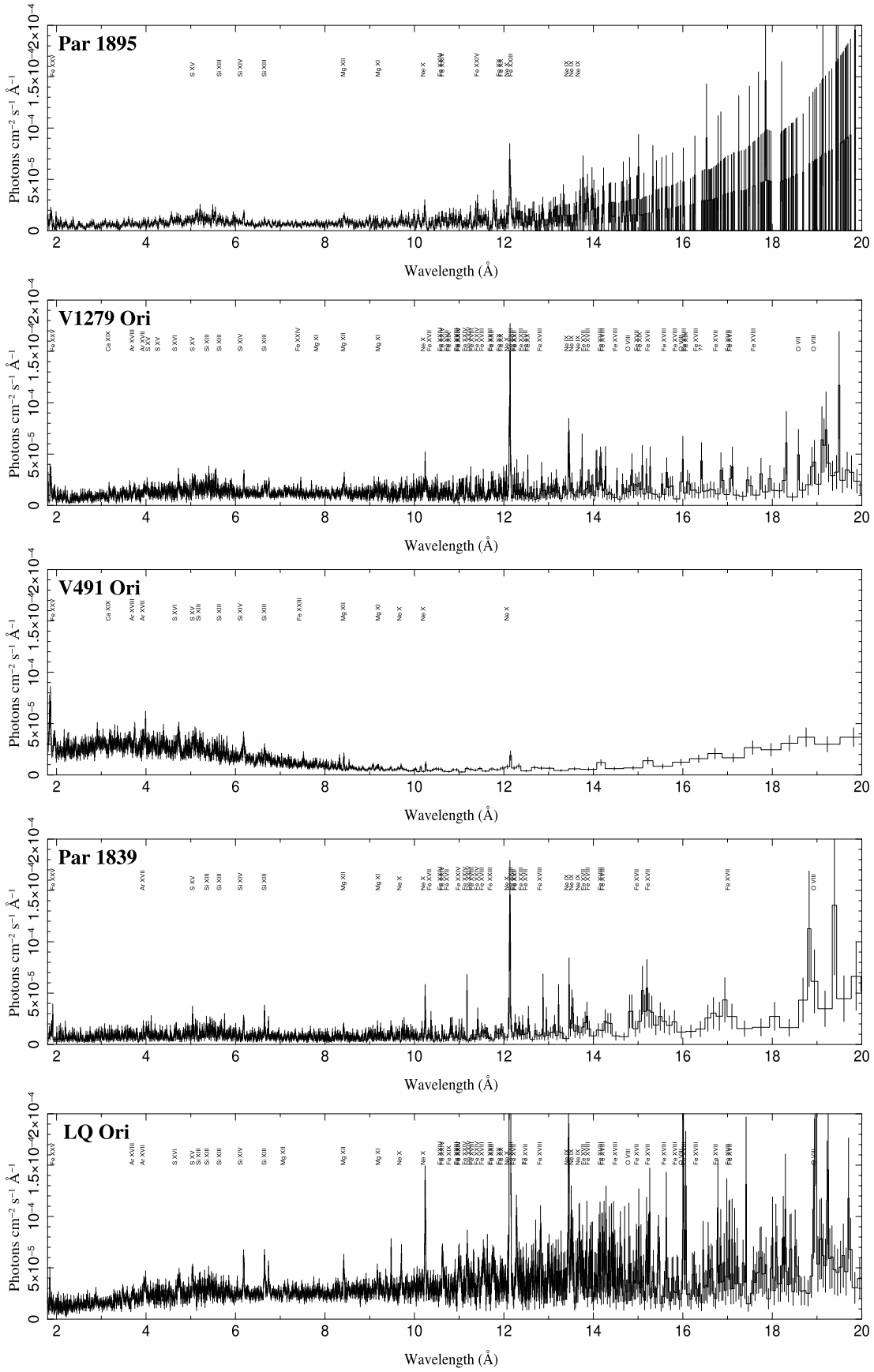

Figure B5. The broadband 2.1 Ms spectra of low- and intermediate-mass stars (continued).

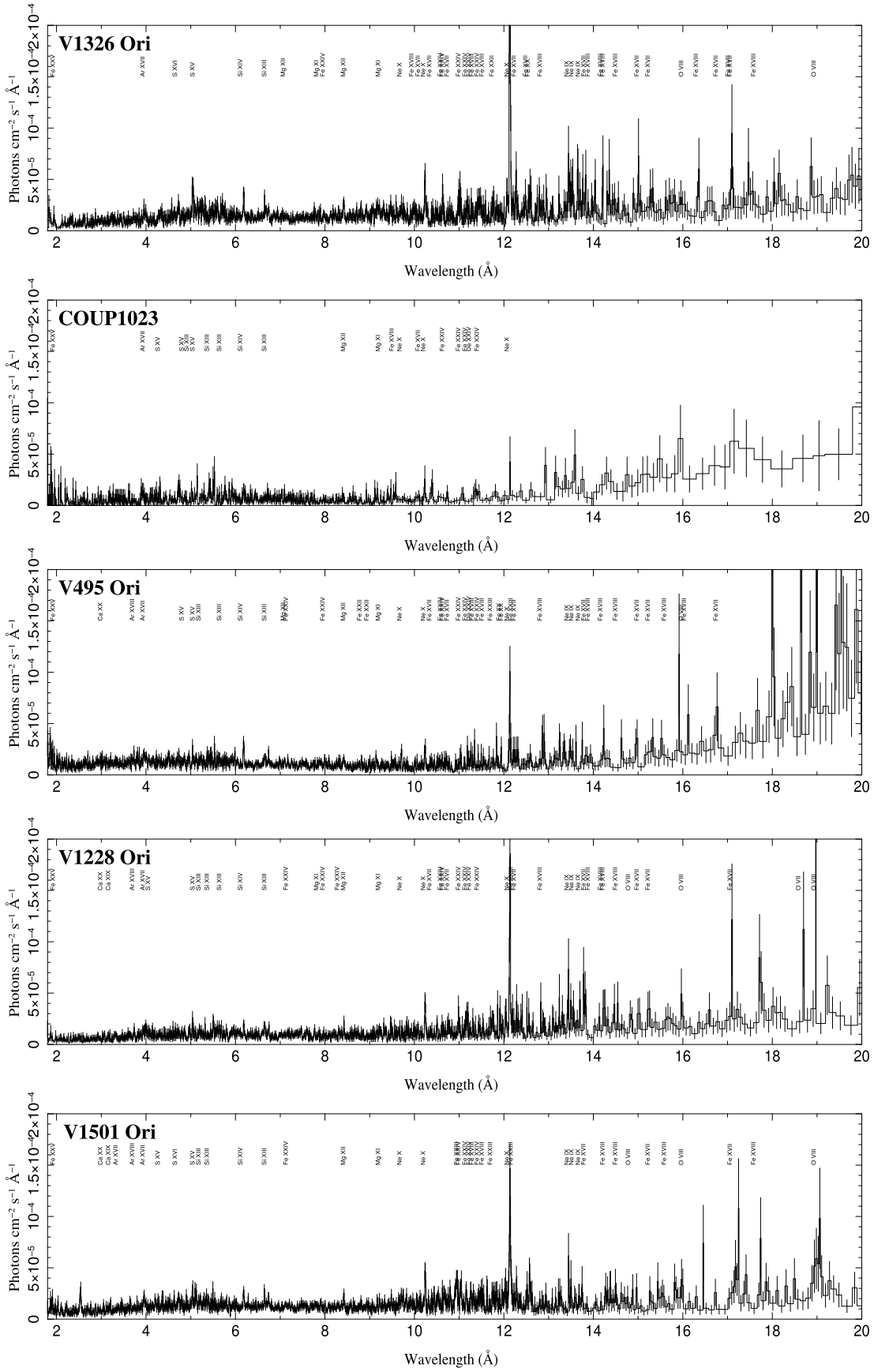

Figure B6. The broadband 2.1 Ms spectra of low- and intermediate-mass stars (continued).

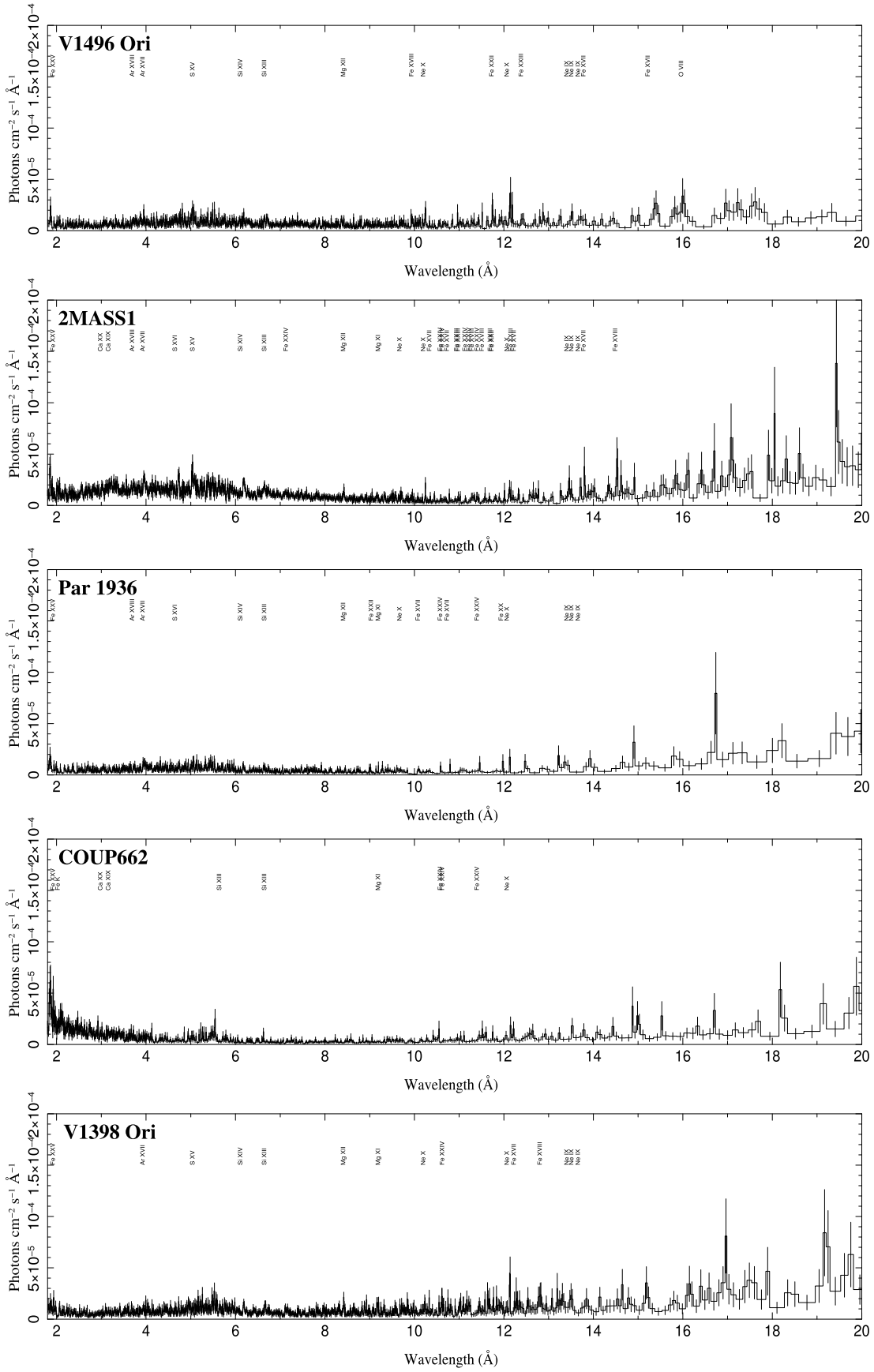

Figure B7. The broadband 2.1 Ms spectra of low- and intermediate-mass stars (continued).

ORCID iDs

Norbert S. Schulz https://orcid.org/0000-0000-0842-7792
David P. Huenemoerder https://orcid.org/0000-0002-3860-6230
Hans Moritz Günther https://orcid.org/0000-0003-4243-2840
Joel Kastner https://orcid.org/0000-0002-3138-8250
Joy Nichols https://orcid.org/0000-0003-3298-7455
Andrew Pollock https://orcid.org/0000-0002-5725-7072
Thomas Preibisch https://orcid.org/0000-0003-3130-7796
Paola Testa https://orcid.org/0000-0002-0405-0668
Fabio Reale https://orcid.org/0000-0002-1820-4824
Claude R. Canizares https://orcid.org/0000-0002-5769-8441

References

Anders, E., & Grevesse, N. 1989, GeCoA, 53, 197
Argiroffi, C., Maggio, A., & Peres, G. 2007, A&A, 465, L5
Argiroffi, C., Maggio, A., Montmerle, T., et al. 2012, ApJ, 752, 100
Bally, J., O'Dell, C. R., & McCaughrean, M. J. 2000, AJ, 119, 2919
Brickhouse, N. S., Cranmer, S. R., Dupree, A. K., Luna, G. J. M., & Wolk, S. 2010, ApJ, 710, 1835
Broos, P. S., Feigelson, E. D., Townsley, L. K., et al. 2007, ApJS, 169, 353
Broos, P. S., Townsley, L. K., Feigelson, E. D., et al. 2011, ApJS, 194, 2
Canizares, C. R., Huenemoerder, D. P., Davis, D. S., et al. 2000, ApJL, 539, L41
Cash, W. 1979, ApJ, 228, 939
Crowther, P. A., Broos, P. S., Townsley, L. K., et al. 2022, MNRAS, 515, 4130
Da Rio, N., Robberto, M., Soderblom, D. R., et al. 2010, ApJ, 722, 1092
den Boggende, A. J. F., Mewe, R., Gronenschild, E. H. B. M., Heise, J., & Grindlay, J. E. 1978, A&A, 62, 1
Espaillat, C. C., Robinson, C. E., Romanova, M. M., et al. 2021, Natur, 597, 41
Fabricius, C., Luri, X., Arenou, F., et al. 2021, A&A, 649, A5
Feigelson, E. D., & Decampli, W. M. 1981, ApJL, 243, L89
Feigelson, E. D., Getman, K., Townsley, L., et al. 2005, ApJS, 160, 379
Feigelson, E. D., Getman, K. V., Townsley, L. K., et al. 2011, ApJS, 194, 9
Fruscione, A., McDowell, J. C., Allen, G. E., et al. 2006, Proc. SPIE, 6270, 62701V
Gagne, M., Caillault, J.-P., & Stauffer, J. R. 1995, ApJ, 445, 280
Gagné, M., Oksala, M. E., Cohen, D. H., et al. 2005, ApJ, 628, 986
Gagné, M., Fehon, G., Savoy, M. R., et al. 2011, ApJS, 194, 5
Getman, K. V., Flaccomio, E., Broos, P. S., et al. 2005, ApJS, 160, 319
Giacconi, R., Murray, S., Gursky, H., et al. 1972, ApJ, 178, 281
GRAVITY Collaboration, Karl, M., Pfuhl, O., et al. 2018, A&A, 620, A116
Gregory, P. C., & Loredo, T. J. 1992, ApJ, 398, 146
Grellmann, R., Preibisch, T., Ratzka, T., et al. 2013, A&A, 550, A82
Grosso, N., Bouvier, J., Montmerle, T., et al. 2007, A&A, 475, 607
Güdel, M., Audard, M., Bacciotti, F., et al. 2011, in ASP Conf. Ser. 448, 16th Cambridge Workshop on Cool Stars, Stellar Systems, and the Sun, ed. C. Johns-Krull, M. K. Browning, & A. A. West (San Francisco, CA: ASP), 617
Günther, H. M., Liefke, C., Schmitt, J. H. M. M., Robrade, J., & Ness, J.-U. 2006, A&A, 459, L29
Günther, H. M., & Schmitt, J. H. M. M. 2008, A&A, 481, 735
Günther, H. M., Schmitt, J. H. M. M., Robrade, J., & Liefke, C. 2007, A&A, 466, 1111
Günther, H. M., Birnstiel, T., Huenemoerder, D. P., et al. 2018, AJ, 156, 56
Hartmann, L., Herczeg, G., & Calvet, N. 2016, ARA&A, 54, 135
Herbig, G. H., & Griffin, R. F. 2006, AJ, 132, 1763
Hillenbrand, L. A. 1997, AJ, 113, 1733
Hillenbrand, L. A., Hoffer, A. S., & Herczeg, G. J. 2013, AJ, 146, 85
Houck, J. C., & Denicola, L. A. 2000, ASP Conf. Ser. 216, Astronomical Data Analysis Software and Systems IX, ed. N. Manset, C. Veillet, & D. Crabtree (San Francisco, CA: ASP), 591
Huenemoerder, D. P., Canizares, C. R., Drake, J. J., & Sanz-Forcada, J. 2003, ApJ, 595, 1131
Huenemoerder, D. P., Kastner, J. H., Testa, P., Schulz, N. S., & Weintraub, D. A. 2007, ApJ, 671, 592
Huenemoerder, D. P., Schulz, N. S., Testa, P., Kesich, A., & Canizares, C. R. 2009, ApJ, 707, 942
Karl, M., Pfuhl, O., Eisenhauer, F., Genzel, R., & Grellmann, R. 2018, A&A, 620, A116
Kastner, J. H., Franz, G., Grosso, N., et al. 2005, ApJS, 160, 511
Kastner, J. H., Huenemoerder, D. P., Schulz, N. S., et al. 2004, ApJL, 605, L49
Kastner, J. H., Huenemoerder, D. P., Schulz, N. S., Canizares, C. R., & Weintraub, D. A. 2002, ApJ, 567, 434
Kastner, J. H., Zuckerman, B., Weintraub, D. A., & Forveille, T. 1997, Sci, 277, 67
Kounkel, M., Hartmann, L., Loinard, L., et al. 2017, ApJ, 834, 142
Kraus, S., Weigelt, G., Balega, Y. Y., et al. 2009, A&A, 497, 195
Kuhn, M. A., Hillenbrand, L. A., Sills, A., Feigelson, E. D., & Getman, K. V. 2019, ApJ, 870, 32
Lamzin, S. A. 1998, ARep, 42, 322
Lindegren, L., Bastian, U., Biermann, M., et al. 2021, A&A, 649, A4
Maggio, A., Flaccomio, E., Favata, F., et al. 2007, ApJ, 660, 1462
Maíz Apellániz, J., Barbá, R. H., Fernández Aranda, R., et al. 2022, A&A, 657, A131
Manara, C. F., Robberto, M., Da Rio, N., et al. 2012, ApJ, 755, 154
Menten, K. M., Reid, M. J., Forbrich, J., & Brunthaler, A. 2007, A&A, 474, 515
Mitschang, A. W., Schulz, N. S., Huenemoerder, D. P., Nichols, J. S., & Testa, P. 2011, ApJ, 734, 14
Morales-Calderón, M., Stauffer, J. R., Stassun, K. G., et al. 2012, ApJ, 753, 149
Muench, A. A., Lada, E. A., Lada, C. J., & Alves, J. 2002, ApJ, 573, 366
Olivares, J., Sarro, L. M., Bouy, H., et al. 2020, A&A, 644, A7
Orlando, S., Sacco, G. G., Argiroffi, C., et al. 2010, A&A, 510, A71
Orlando, S., Bonito, R., Argiroffi, C., et al. 2013, A&A, 559, A127
Petr, M. G., Coudé du Foresto, V., Beckwith, S. V. W., Richichi, A., & McCaughrean, M. J. 1998, ApJ, 500, 825
Pillitteri, I., Wolk, S. J., Megeath, S. T., et al. 2013, ApJ, 768, 99
Preibisch, T., Balega, Y., Hofmann, K.-H., Weigelt, G., & Zinnecker, H. 1999, NewA, 4, 531
Preibisch, T., Hodgkin, S., Irwin, M., et al. 2011, ApJS, 194, 10
Principe, D. A., Sacco, G., Kastner, J. H., Stelzer, B., & Alcalá, J. M. 2016, MNRAS, 459, 2097
Reale, F., Orlando, S., Testa, P., Landi, E., & Schrijver, C. J. 2014, ApJL, 797, L5
Reale, F., Orlando, S., Testa, P., et al. 2013, Sci, 341, 251
Robberto, M., Soderblom, D. R., Scandariato, G., et al. 2010, AJ, 139, 950
Robrade, J., & Schmitt, J. H. M. M. 2006, A&A, 449, 737
Robrade, J., & Schmitt, J. H. M. M. 2007, A&A, 473, 229
Rots, A. H. 2012, in IAU Symp. 285, New Horizons in Time Domain Astronomy, ed. E. Griffin, R. Hanisch, & R. Seaman, 402
Rzaev, A. K., Shimansky, V. V., & Kolbin, A. I. 2021, MNRAS, 504, 3787
Sacco, G. G., Orlando, S., Argiroffi, C., et al. 2010, A&A, 522, A55
Schmitt, J. H. M. M., Robrade, J., Ness, J.-U., Favata, F., & Stelzer, B. 2005, A&A, 432, L35
Schneider, P. C., France, K., Günther, H. M., et al. 2015, A&A, 584, A51
Schneider, P. C., Günther, H. M., Robrade, J., Schmitt, J. H. M. M., & Güdel, M. 2018, A&A, 618, A55
Schneider, P. C., Günther, H. M., & Ustamujic, S. 2022, in Handbook of X-ray and Gamma-ray Astrophysics, ed. C. Bambi & A. Santangelo (Berlin: Springer)
Schulz, N. S., Canizares, C., Huenemoerder, D., & Tibbets, K. 2003, ApJ, 595, 365
Schulz, N. S., Canizares, C. R., Huenemoerder, D., & Lee, J. C. 2000, ApJL, 545, L135
Schulz, N. S., Huenemoerder, D. P., Günther, M., Testa, P., & Canizares, C. R. 2015, ApJ, 810, 55
Schulz, N. S., Testa, P., Huenemoerder, D. P., Ishibashi, K., & Canizares, C. R. 2006, ApJ, 653, 636
Skrutskie, M. F., Cutri, R. M., Stiening, R., et al. 2006, AJ, 131, 1163
Telleschi, A., Güdel, M., Briggs, K. R., Audard, M., & Palla, F. 2007, A&A, 468, 425
Testa, P., Drake, J. J., & Peres, G. 2004, ApJ, 617, 508
Townsley, L. K., Broos, P. S., Feigelson, E. D., et al. 2006, AJ, 131, 2140
Townsley, L. K., Broos, P. S., Corcoran, M. F., et al. 2011, ApJS, 194, 1
Tsuboi, Y., Koyama, K., Murakami, H., et al. 1998, ApJ, 503, 894
Vilhu, O. 1984, A&A, 133, 117
Vilhu, O., & Walter, F. M. 1987, ApJ, 321, 958
Vuong, M. H., Montmerle, T., Grosso, N., et al. 2003, A&A, 408, 581
Waldron, W. L., Cassinelli, J. P., Miller, N. A., MacFarlane, J. J., & Reiter, J. C. 2004, ApJ, 616, 542
Wang, J., Townsley, L. K., Feigelson, E. D., et al. 2007, ApJS, 168, 100
Wang, J., Townsley, L. K., Feigelson, E. D., et al. 2008, ApJ, 675, 464
Wolk, S. J., Spitzbart, B. D., Bourke, T. L., & Alves, J. 2006, AJ, 132, 1100
Wright, N. J., Drake, J. J., Mamajek, E. E., & Henry, G. W. 2011, ApJ, 743, 48